Point defect structures in hexagonal close packed metals and across the Periodic Table

Andrew R. Warwick, Pui-Wai Ma, and Sergei L. Dudarev
United Kingdom Atomic Energy Authority, Culham Campus, Oxfordshire OX14 3DB, United Kingdom

(Received 27 May 2025; accepted 20 August 2025; published 30 September 2025)

We present a comprehensive *ab initio* dataset of formation energies and elastic properties of intrinsic point defects across all the transition and rare earth hexagonal close packed (hcp) metals, as well as metalloid elements with hcp crystal structure. Point defect properties appear weakly correlated with the c/a ratio of the hcp lattice. Instead, it is the position of an element in the Periodic Table that primarily defines the relaxation volume tensor, elastic dipole tensor, and formation energy of a point defect. This suggests that the local variations in the electronic structure and interatomic bonding at the core of a defect dominate its properties, as opposed to long-range elastic deformations of the lattice. Across all the metals, we find that the relaxation volumes of vacancies and self-interstitial defects are correlated with atomic volumes, with values of -0.35 and 1.46 atomic volumes for a vacancy and a self-interstitial defect, respectively, providing a universally good approximation independent of the crystal structure. This study complements and completes the existing point defect databases spanning body-centered cubic and face-centered cubic metals.

DOI: 10.1103/qmfp-j51l

I. INTRODUCTION

Properties of metals are sensitive to perturbations of their underlying crystal structure. Intrinsic point defects are the simplest types of lattice defects, involving the removal or insertion of a single atom. Vacancies and self-interstitial atom (SIA) defects are readily created, for example, by high-energy particle irradiation in a nuclear reactor. Their coalescence into larger, extended defects, such as dislocations and voids, is among the causes of hardening and embrittlement. The accumulation of point defects also gives rise to dimensional changes and swelling.

Defects interact through long-range elastic fields, with the strength of interaction determined by elastic dipole tensors P_{ij} ([1], p. 161). A sample of the host metal, free from body forces and tractions, changes shape and volume according to the relaxation volume tensor $\Omega_{ij} = S_{ijkl}P_{kl}$ [2,3] of the defects contained in it, where S_{ijkl} is the elastic compliance tensor ([4], p. 29). Models for microstructural evolution at larger length scales, treating interactions between the defects, require these tensorial quantities as input. Compiling a database of point defect elastic tensors is a necessary step involved in predicting deformations of materials operating in an irradiation environment.

P_{ij} and Ω_{ij} for a vacancy and various SIA configurations have been computed *ab initio* and tabulated across all the body centered cubic (bcc) [2] and face centered cubic (fcc) [3] metals, except the lanthanides and actinides. The lowest-energy SIA structure in all the bcc metals has the $\langle 111 \rangle$ symmetry, except magnetic Fe [5]. In Cr, Mo, and W the $\langle 111 \rangle$ symmetry is slightly broken by the buckling occurring in the core of the defect [6,7]. In fcc metals, the $\langle 100 \rangle$ dumbbell is often, but not always, the lowest-energy SIA configuration.

A compilation of point defect elastic dipole and relaxation volume tensors for the hexagonal close packed (hcp) metals is currently missing. Many hcp metals play an important role in engineering applications such as lightweight structural components composed of Mg [8] or Ti [9], Zr nuclear fuel claddings [10], and Be as a candidate neutron multiplier material in nuclear fusion reactors [11].

Until now, Pasianot [12] has conducted the most comprehensive *ab initio* study of elastic properties of point defects in hcp metals. The trends in the defect formation energy, dipole tensors, and relaxation volumes with respect to the c/a ratio were explored and compared to resistivity recovery, internal friction, and Huang diffuse x-ray scattering (DXS) data. Seven elements were included in the study [12]: the two elements that have a larger than ideal c/a ratio, Cd and Zn, as well as Be, Ti, Zr, Mg, and Co. For Be, Ti, and Zr, the lowest formation energy SIA was found to be the basal octahedral (BO) configuration, with Mg and Co instead favoring the crowdion (C) and [0001] split dumbbell (S) defect structure, respectively. The SIA formation energies computed for Cd and Zn showed a clear preference for the out-of-basal-plane configurations over the basal SIAs. Due to the ease of transformation of the ground state configuration of the defect into alternative configurations, it was suggested that SIA migration is likely to be three dimensional in Zn, Cd, and Mg. The predicted values of P_{ij} were compared with Huang DXS measurements, suggesting that the computed and experimentally measured values were often not compatible with each other. Dipole tensor calculations have also been performed for the group IV hcp metals Ti, Zr, and Hf [13], showing that in Zr the SIA configurations with monoclinic symmetry had the lowest energy and were consistent with internal friction experimental measurements. The elastic properties of defects across the

Published by the American Physical Society under the terms of the Creative Commons Attribution 4.0 International license. Further distribution of this work must maintain attribution to the author(s) and the published article's title, journal citation, and DOI.

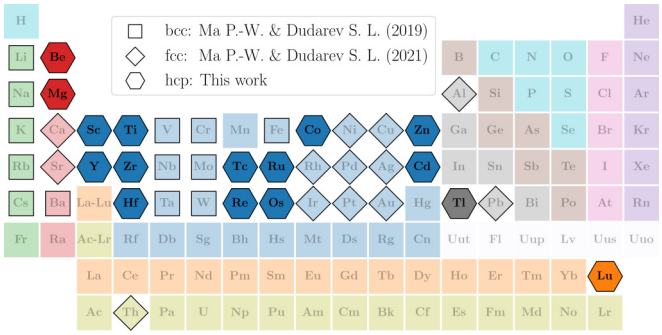


FIG. 1. The elements with hcp structure considered in this work and highlighted by hexagon cells. The bcc [2] and fcc [3] metals considered in previous studies are depicted by the bordered squares and diamonds, respectively. Most of the lanthanide and actinide hcp metals were not included in this study.

Periodic Table have also been investigated using embedded atom method (EAM) potentials [14–16], which often exhibit relatively poor accuracy in comparison with *ab initio* calculations.

Most studies of defects in hcp metals have focused on formation and migration energies [17]. Of particular note are the *ab initio* high-throughput calculations conducted by Shang *et al.* [18] that have yielded a complete database of energies for vacancy defects across *all* the elements in the Periodic Table, including the elements with hcp crystal structure. Self-interstitial atom defects have been investigated, using *ab initio* methods, in Zn [19], Be [20,21], Y [22], Ti [13,23–26], Zr [13,27–38], Mg [39], Dy [40], Hf [13], and Sc [41]. The results are broadly consistent with an earlier hypothesis that the SIAs lying in the basal plane are the most stable configurations in all the hcp elements with the lower than ideal c/a ratio [42].

In this study, we compute the formation energies, dipole tensors, and relaxation volume tensors of defects in all the hcp metals and hcp metalloid elements in the Periodic Table, with the exception of lanthanides and actinides, shown in Fig. 1 by the hexagon symbols. The bcc [2,7] and fcc [3] metals studied earlier are denoted by squares and diamonds, respectively. We analyse the relative contributions of long range elastic fields and short range electronic structure distortions to the energy of defects in Sec. II A followed by an outline of the point defect configurations and simulations methods in Sec. II B. A tabulation and analysis of our results is presented in Sec. III. The hcp point defect data presented here are combined with prior bcc [2] and fcc [3] results, with detailed analysis in Sec. IV and conclusions in Sec. V.

II. METHODOLOGY

A. Electronic structure versus elasticity effects

When investigating the structure of defects formed in materials by irradiation, it is natural to start the analysis from assessing the relative contributions to the energy of defects stemming from long-range elastic strain fields and from the transformation of local electronic states arising from strong anharmonic deformations of atomic configuration in the core of a defect. It is not immediately evident what contribution dominates the total energy. For example, in the treatment of mesoscopic dislocation loops and line dislocations, it has always been assumed that the energy of the defect has elastic origin [43], namely,

$$E_{\rm el} = \frac{1}{2}\int_V C_{ijkl}\epsilon_{ij}(\mathbf{r})\epsilon_{kl}(\mathbf{r})d^3r, \tag{1}$$

where repeated indexes imply summation, and the indices themselves refer to Cartesian coordinates. Integration is performed over the entire volume of a solid body excluding the core region of the defect, C_{ijkl} is the four-index elastic stiffness tensor [44], and

$$\epsilon_{ij}(\mathbf{r}) = \frac{1}{2}\left[\frac{\partial u_i(\mathbf{r})}{\partial x_j} + \frac{\partial u_j(\mathbf{r})}{\partial x_i}\right] \tag{2}$$

is the symmetrized tensor of partial derivatives of the field of displacements with respect to coordinates $\mathbf{r} = (x_1, x_2, x_3)$, known as the strain tensor [4,45].

In an elastically isotropic material, the elastic stiffness tensor has the form [4]

$$C_{ijkl} = \mu\frac{2\nu}{1-2\nu}\delta_{ij}\delta_{kl} + \mu(\delta_{ik}\delta_{jl} + \delta_{il}\delta_{jk}), \tag{3}$$

where μ is the shear modulus and ν is the Poisson ratio. In this approximation, the field of elastic displacements produced by a point defect situated at the origin can be represented in an explicit analytical form as [46]

$$u_i(\mathbf{r}) = \frac{1}{16\pi\mu(1-\nu)}\frac{1}{r^2}[2(1-2\nu)P_{il}\eta_l - \eta_i P_{kk} + 3\eta_i(\eta_k P_{kl}\eta_l)]. \tag{4}$$

Here $\boldsymbol{\eta} = \mathbf{r}/r$ and P_{kl} is the elastic dipole tensor of the defect [1].

The most significant, from the perspective of evaluating the energy of a defect, aspect of Eq. (4) is the variation of elastic strain field as a function of distance from the center of the defect,

$$\epsilon_{ij}(\mathbf{r}) = \frac{a_{ij}(\boldsymbol{\eta})}{r^3}, \tag{5}$$

where the tensorial factor $a_{ij}(\boldsymbol{\eta})$, deducible from (4), is a function of the direction of $\mathbf{r}$ but not of its magnitude. Substituting (5) into (1), we arrive at

$$E = \frac{1}{2}C_{ijkl}\int_V \frac{a_{ij}(\boldsymbol{\eta})a_{kl}(\boldsymbol{\eta})}{r^6}d^3r = \frac{1}{2}C_{ijkl}\int_{4\pi} a_{ij}(\boldsymbol{\eta})a_{kl}(\boldsymbol{\eta})d\Omega\int_{r_c}^{R}\frac{dr}{r^4}, \tag{6}$$

where in the second line we separated integration over the solid angle from the integration over the radial coordinate. The latter varies from the core radius of the defect r_c to the outer boundary R of the solid body [47]. In all the practical cases referring to point defects, r_c is of the order of a nanometer and R is macroscopic; hence $r_c \ll R$.

Integrating over r in (6), we find that the total energy of a point defect depends on the core radius r_c as

$$E \sim r_c^{-3}. \tag{7}$$

While the definition of the core radius is to some extent arbitrary, the above estimate shows that for a localized defect

object, for example, a vacancy or a self-interstitial atom, the dominant contribution to the total energy comes overwhelmingly from the central strongly distorted part of the defect structure. Even though the above derivation is based on the theory of elasticity argument (1), the functional form of (7) suggests that the far-field elastic contribution to the energy of a point defect is effectively negligible. In other words, the energy of a defect arises primarily from changes in the local electronic structure in the core of the defect, where electronic configurations differ dramatically from those of the surrounding material. The small correction term coming from the upper limit of integration in (6) is proportional to R^{-3}. This correlates with the variation of energy as a function of simulation cell size and number of atoms N in the cell as $E \sim R^{-3} \sim N^{-1}$ found in the convergence analysis performed in Ref. [48] and in our study below. As a side note, the elastic part of the total energy of a line dislocation depends on the core radius logarithmically $E \sim \mu b^2 \ln(R/r_c)$; see Eq. (6.38) of Ref. [4]. This is different from the case of a point defect, and for a line dislocation, the elastic part of the total energy is comparable to the contribution from the electronic structure effects in the dislocation core.

The dominance of electronic structure contribution to the energy of a point defect, as opposed to elastic self-energy, explains why properties of defects in elemental solids are correlated with the position of a chemical element in the Periodic Table [5]. This also agrees with the lack of notable correlation between elastic properties of elements and point defect energies noted in Ref. [49].

In view of the above, we now proceed to the investigation of structure and stability of defects, using an electronic-structure-based *ab initio* approach.

B. Density functional theory calculations

Density functional theory (DFT) calculations were performed using the Vienna *Ab initio* Simulation Package (VASP) version 6.4.1 [51–54]. In Table I we summarize the selected plane-wave energy cutoff E_{cut}, k-point mesh, and valence electron configuration of the plane augmented wave (PAW) pseudopotential [55,56] for each hcp metal. For a given element, we have chosen the pseudopotential with the lowest number of core electrons, to achieve the highest possible accuracy in the treatment of interatomic interactions at short distances in the SIA structures. The results of convergence tests are given in the Supplemental Material [57]. The energies computed by the self-consistent field method were converged to within 10^{-8} eV and the point defect structures were relaxed until the maximum magnitude of force on any atom was smaller than 0.01 eV/Å. The Perdew-Burke-Ernzerhof (PBE) exchange-correlation functional E_{xc} [58] was employed for all the hcp elements. For Be, Zn, and Cd, the PBEsol functional [59] was also considered, as discussed in Sec. III. Otherwise, earlier studies have shown that various choices for E_{xc} often do not have a significant effect on the resulting elastic dipole tensors [2,3].

Bulk lattice parameters were optimized such that the change in energy between the successive ionic relaxation steps in calculations of perfect lattice structures was less than 10^{-7} eV. As shown in Fig. 2, the predicted lattice parameters are in good agreement with experiment data [50], and the relative error of either a or c with respect to experiment does not exceed 5%. Furthermore, the predicted c/a ratios differ from experimental values by less than 3%.The elastic constants were computed via the symmetrized finite differences method [65,66]. In general, the relative differences between the predicted and measured elastic constants [60–64] are satisfactory (see Fig. 3). The largest relative error appears in the C_{12} elastic constant of Be, for which the experimental value is $C_{12} = 27.6$ GPa [60]. We note, however, that the absolute error in this case is still similar to the scale of discrepancies found across all the hcp elements.

TABLE I. Parameters for atomic relaxation simulations performed using vasp in the PBE approximation for the exchange-correlation functional. E_{cut} is the plane-wave cutoff energy and k grid denotes the Γ-centered evenly spaced k-point mesh utilized for a two-atom hcp primitive cell.

Element	Valence electrons	E_{cut} (eV)	k grid
Be	$1s^2 2s^2$	800	19×19×12
Mg	$2s^2 2p^6 3s^2$	1000	17×17×11
Sc	$3s^2 3p^6 4s^1 3d^2$	700	11×11×07
Y	$4s^2 4p^6 5s^1 4d^2$	400	17×17×11
Lu	$5s^2 5p^6 4f^{14} 6s^2 5d^1$	600	13×13×08
Ti	$3s^2 3p^6 4s^1 3d^3$	600	15×15×09
Zr	$4s^2 4p^6 5s^1 4d^3$	700	17×17×11
Hf	$5s^2 5p^6 5d^4$	700	17×17×11
Tc	$4p^6 4d^6 5s^1$	800	19×19×12
Re	$5p^6 6s^1 5d^6$	600	19×19×12
Ru	$4s^2 4p^6 4d^7 5s^1$	900	17×17×11
Os	$5p^6 6s^1 5d^7$	600	17×17×11
Co	$3s^2 3p^6 4s^1 3d^8$	900	19×19×12
Zn	$3d^{10} 4s^2$	700	17×17×11
Cd	$4d^{10} 5s^2$	700	17×17×09
Tl	$5d^{10} 6s^2 6p^1$	900	17×17×11

Ferromagnetic hcp Co was treated in the collinear magnetic approximation, similarly to the treatment of ferromagnetic bcc Fe and antiferromagnetic bcc Cr [2], and ferromagnetic fcc Ni [3]. The calculated magnetic moment of 1.616 μ_B per Co atom is in good agreement with the experimentally measured value of 1.71 μ_B per atom [67].

The formation energies $E^{\text{F}}_{\text{def}}$ and elastic dipole tensors of a vacancy and five self-interstitial atom defect configurations were computed for each chemical element. The formation energy of a defect is defined as

$$E^{\text{F}}_{\text{def}} = [E_{\text{def}}(N_{\text{def}}) - E^{\text{app}}] - \frac{N_{\text{def}}}{N_{\text{perf}}} E_{\text{perf}}(N_{\text{perf}}) - E^{\text{corr}}_{\text{el}}, \quad (8)$$

where the energy of a simulation cell containing a defect in a configuration of the total of N_{def} atoms is E_{def}, and the corresponding perfect lattice reference cell containing N_{perf} atoms is E_{perf}. For a vacancy or a self-interstitial atom defect, $N_{\text{def}} - N_{\text{perf}}$ is -1 or $+1$, respectively. E^{app} is the energy associated with externally applied strain and $E^{\text{corr}}_{\text{el}}$ is the energy of elastic interaction between a defect and all the periodic images of it. Accounting for the energy of interaction with periodic images of defect structures $E^{\text{corr}}_{\text{el}}$ is possible [68],

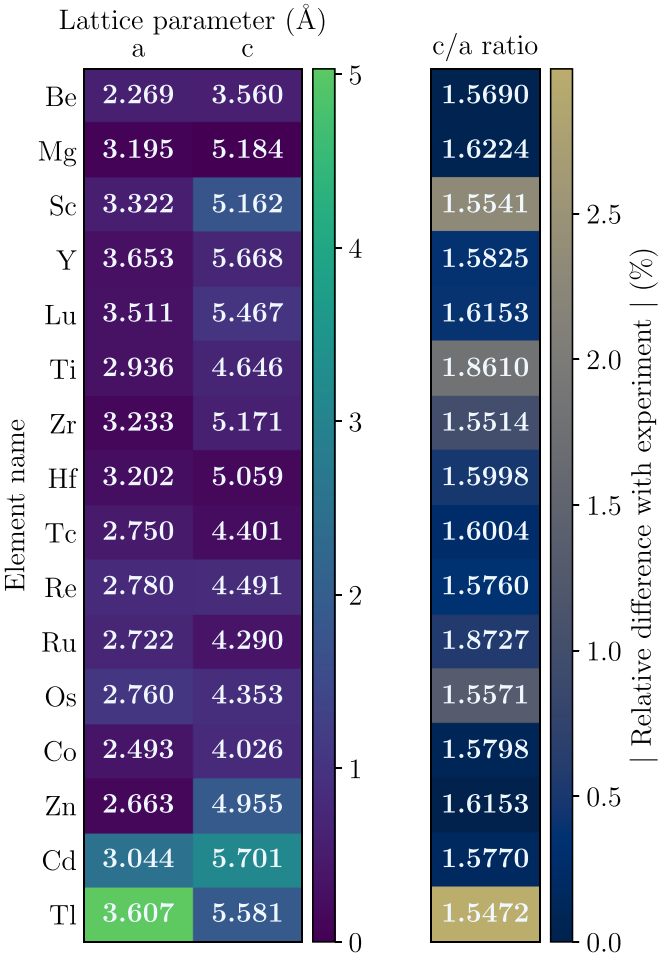


FIG. 2. *Ab initio* predicted values of lattice parameters and c/a ratios for all the hcp elements included in this study. The cells in the table are colored according to the absolute difference between the calculated values and experimental measurements. Experiment data are sourced from Ref. [50] and are the 0 K values, with the exception of Hf for which the lowest-temperature experimental values correspond to room temperature.

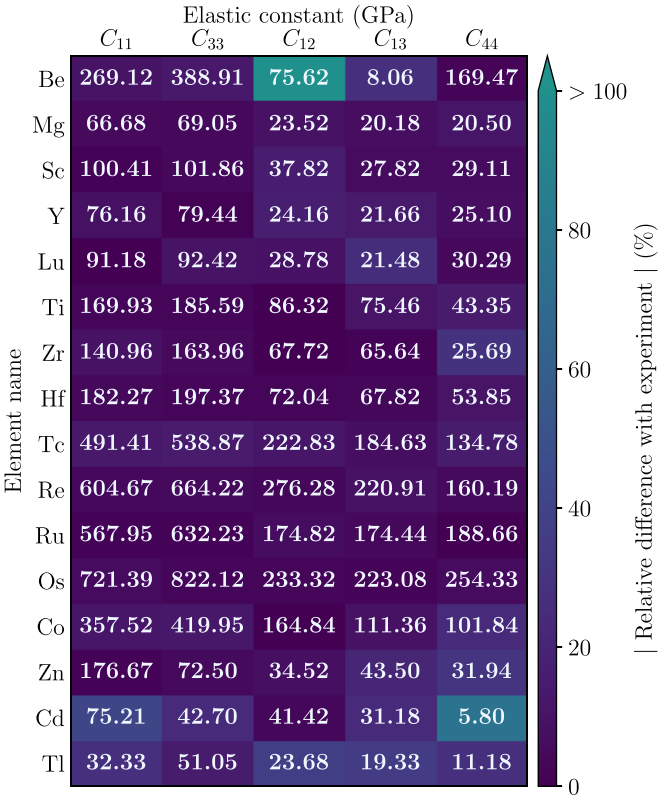


FIG. 3. *Ab initio* predicted values of elastic constants for all the hcp elements included in this study. Cells in the table are colored according to the absolute difference between the calculated values and experimental measurements. Experiment data are sourced from Simmons and Wang [60] for temperatures less than 4 K for all the elements, with the exception of Lu [61] (4 K), Os [62] (5 K), Sc [63] (300 K), and Tc [64] (298 K).

and the corresponding correction term was computed using the CALANIE program [69]. Further details may be found in Refs. [2,3].

We constructed simulation cells from repeats of the two-atom hcp primitive cell with space group 194 $P6_3/mmc$ and occupied Wyckoff position $c = (1/3, 2/3, 1/4)$ ([70], Chap. 2.3). Both atoms in the primitive cell belong to the orbit of a single Wyckoff position. It follows that the structure and tensorial properties of a vacancy at either site in the primitive cell are related by a symmetry operation of the crystal space group. Thus there is only one type of vacancy defect in an hcp crystal. Conversely, multiple nonequivalent SIA geometries need to be considered. The relaxed configurations of the basal octahedral (BO), basal $\langle 2\bar{1}\bar{1}0\rangle$ split dumbbell (BS), octahedral (O), $\langle 0001\rangle$ split dumbbell (S), and crowdion (C) SIAs for Zr are shown in Fig. 4. Vérité *et al.* [13] and Pasianot [12] have highlighted the important role of low-symmetry defect configurations in determining the migration pathways of SIAs. For certain low-symmetry configurations, the formation energy was found to be only slightly above the lowest-energy high-symmetry SIA configuration. Here, we present only the high-symmetry initial configurations so that the configurational and energy landscape of SIAs across all the hcp metals may be explored efficiently. The high-symmetry tetrahedral (T), basal tetrahedral (BT), and basal crowdion (BC) defects were not included in this study for reasons similar to those given by Pasianot [12] and Vérité *et al.* [13]. Across many hcp metals, we found that T relaxes into a $\langle 0001\rangle$ split dumbbell SIA. For the BC configuration, the self-consistent field cycles are often unable to converge if either BS or BO structures did not emerge instead. BT possesses a formation energy that is substantially higher than the lowest formation energy SIA. For instance, the formation energy of BT in zinc and zirconium was found to be 3.11 and 3.90 eV, respectively, whereas the lowest SIA energy found in Zn was 1.24 eV (octahedral) and for Zr was 2.69 eV (basal octahedral). Similar phenomena have been reported in other *ab initio* hcp point defect studies where, for example, a tetrahedral SIA was often found to spontaneously decay into a different configuration [13,21] or be among the highest SIA formation energies reported for that metal [20,22].

Consider a simulation cell containing a single point defect in a cell containing the total of N_{def} atoms. The structure of

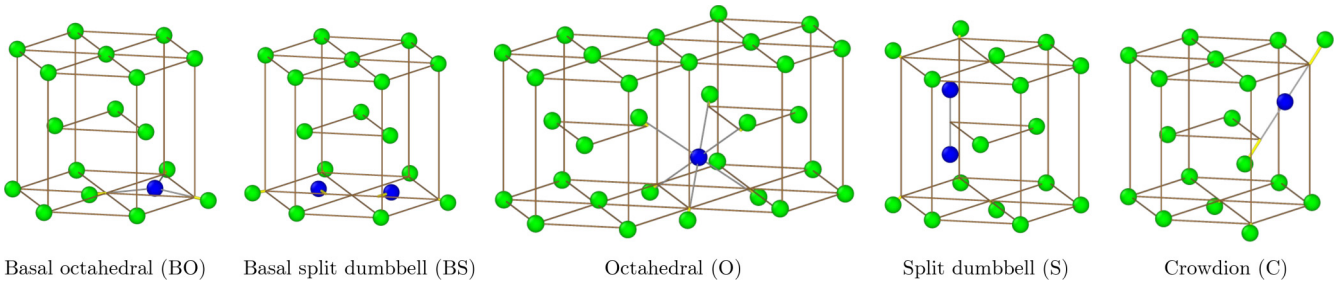


FIG. 4. From left to right: relaxed configurations of the basal octahedral (BO), basal $[2\bar{1}\bar{1}0]$ split dumbbell (BS), octahedral (O), [0001] split dumbbell (BS), and crowdion (C) SIAs for Zr. The inserted atom, or a pair of dumbbell atoms sharing an atomic site, are highlighted in blue. Atomic displacements from the initial configuration are indicated by yellow arrows.

the defect is relaxed under the condition that the cell shape and size are fixed. The dipole tensor $P_{ij}(N_{\rm def})$ is then evaluated from the average residual stress in the cell $\bar{\sigma}_{ij}$ as [68,71]

$$P_{ij}(N_{\rm def}) = -V\bar{\sigma}_{ij}, \tag{9}$$

where V is the volume of the cell. At large distances, the stress field of a defect varies as the inverse cube of the distance from its center $||\sigma_{ij}(\mathbf{r})|| \sim 1/r^3$ [4]. Hence each defect configuration was relaxed using at least three cells containing different number of atoms N. The dipole tensor components were then extrapolated to the limit of infinite cell size to obtain the asymptotic values P_{ij}^{∞} via a least squares fit with respect to a linear function of $1/N$, such that [38,48]

$$P_{ij}(N) = \frac{\alpha_{ij}}{N} + P_{ij}^{\infty}, \tag{10}$$

where α_{ij} is a fitted constant. Often, we found that the reference supercell, representing the relaxed perfect crystal, contained some remnant stress, stemming from the approximations involved in the numerical relaxation procedure. In this way, we have computed the stress of the initial perfect crystal supercell and subtracted it from the elastic-interaction-corrected dipole tensor for each cell size before performing the $1/N$ extrapolation. The number of repeats along each lattice vector were chosen such that the cell edge lengths were approximately equal, resulting in 36-, 96-, and 150-atom cells arising from the 3×3×2, 4×4×3, and 5×5×3 unit cell repeats, respectively. Due to the large c/a ratio of Zn and Cd, a 64-atom 4×4×2 cell was considered in place of a 96-atom 4×4×3 cell. Where computational resources were available, relaxations were also performed on larger cell sizes. For many of the transition hcp metals, we found that Eq. (10) provided a good fit to the point defect data. However, Be, Mg, Zn, Cd, and Tl presented less-optimal fits. In order to maintain consistency, we have presented the result of applying the procedure described above to all elements.

Relaxation volume tensors of isolated point defects Ω_{ij} were computed from the corresponding extrapolated dipole tensors P_{ij}^{∞} via

$$\Omega_{ij} = S_{ijkl}P_{kl}^{\infty}. \tag{11}$$

Unless stated otherwise, we express Ω_{ij} in the atomic volume units Ω_0 for the respective hcp metal, where for the hcp crystal structure $\Omega_0 = \frac{\sqrt{3}}{4}a^2c$. Example extrapolations for the elastic dipole tensors of a Zr vacancy and a Zn crowdion are shown in Fig. 5. Extrapolations for other elements and defect configurations are given in the Supplemental Material [57].

III. RESULTS

The formation energies E_f, elastic dipole tensors P_{ij}, and relaxation volume tensors Ω_{ij} for point defects across all hcp metals highlighted in Fig. 1 are summarized in Tables II–XX. In Secs. III A and III B, we analyze the properties of vacancies and SIAs, respectively. Our values for the dipole and relaxation volume tensors of defects included in the study by Pasianot [12] agree with the values computed there.

A. Vacancies

The vacancy formation energies (see Fig. 6) found in our study agree with those computed by Shang *et al.* [18] within 0.2 eV for all the elements except beryllium where our value for the vacancy formation energy $E_F^{\rm Vac} = 0.16$ eV is significantly lower than 0.92 eV found in Ref. [18], Table III. The discrepancy may be a result of our choice of $E_{\rm cut}$, k-point

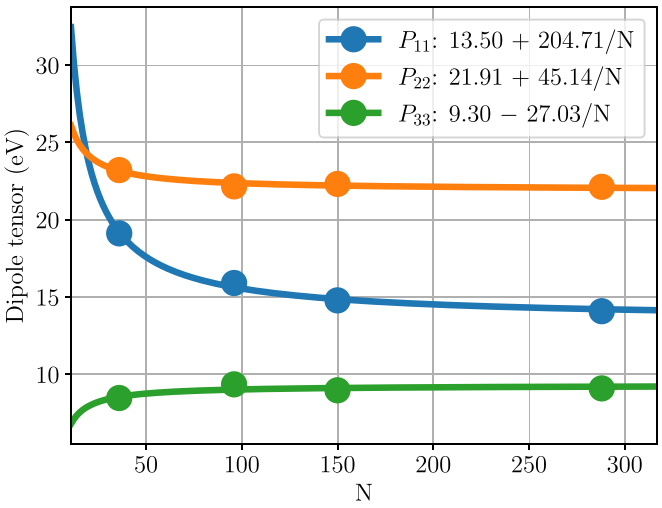


FIG. 5. Example linear extrapolation of dipole tensor components with respect to N, where N denotes the number of atoms in the reference supercell, for a basal $[2\bar{1}\bar{1}0]$ split dumbbell SIA defect in Zr. Cell shape and volume are fixed during internal atomic relaxation. The $1/N$ variation comes from the fact that interaction of a defect with its periodically translated images varies as the inverse cube of the linear dimensions of the cell [48,68].

TABLE II. Beryllium (Be) point defect dipole tensor data computed using the GGA-PBE functional. Formation energy E^F is given in eV units, dipole tensor components P_{ij} are also in eV units, and relaxation volume tensor components Ω_{ij} and their trace $\Omega_{\text{rel}} = \Omega_{ii}$ are given in atomic volume units.

Be_PBE	E^F	P_{11}	P_{22}	P_{33}	P_{12}	P_{23}	P_{31}	Ω_{11}	Ω_{22}	Ω_{33}	Ω_{12}	Ω_{23}	Ω_{31}	Ω_{rel}
Vac	0.610	−4.004	−4.004	3.684	0.000	0.000	0.000	−0.239	−0.239	0.201	0.000	0.000	0.000	−0.277
BO	3.900	18.692	18.692	−5.766	0.000	0.000	0.000	1.103	1.103	−0.345	0.000	0.000	0.000	1.861
BS	4.210	19.214	18.008	−5.331	0.000	0.000	0.000	1.161	1.035	−0.322	0.000	0.000	0.000	1.873
C	4.330	21.923	12.302	0.273	5.402	8.208	9.356	1.505	0.501	−0.027	1.127	0.978	1.115	1.979
O	5.130	16.508	16.508	1.730	0.000	0.000	0.000	0.966	0.966	0.050	0.000	0.000	0.000	1.981
S	5.280	7.500	7.500	23.420	0.000	0.000	0.000	0.411	0.411	1.199	0.000	0.000	0.000	2.021

TABLE III. Beryllium (Be) point defect dipole tensor data computed using the GGA-PBEsol functional. Formation energy E^F is given in eV units, dipole tensor components P_{ij} are also in eV units, and relaxation volume tensor components Ω_{ij} and their trace $\Omega_{\text{rel}} = \Omega_{ii}$ are given in atomic volume units.

Be_PBEsol	E^F	P_{11}	P_{22}	P_{33}	P_{12}	P_{23}	P_{31}	Ω_{11}	Ω_{22}	Ω_{33}	Ω_{12}	Ω_{23}	Ω_{31}	Ω_{rel}
Vac	0.580	−4.787	−4.787	5.004	0.000	0.000	0.000	−0.277	−0.277	0.260	0.000	0.000	0.000	−0.294
BO	4.250	15.675	15.675	−1.025	0.000	0.000	0.000	0.901	0.901	−0.065	0.000	0.000	0.000	1.736
BS	4.350	16.399	16.441	−1.371	0.000	0.000	0.000	0.942	0.945	−0.084	0.000	0.000	0.000	1.803
C	4.470	18.945	11.035	4.037	4.742	6.850	8.214	1.104	0.615	0.194	0.586	0.852	1.022	1.912
S	5.340	3.666	3.666	30.178	0.000	0.000	0.000	0.198	0.198	1.539	0.000	0.000	0.000	1.935
O	5.500	14.647	14.647	4.058	0.000	0.000	0.000	0.839	0.839	0.195	0.000	0.000	0.000	1.874

TABLE IV. Magnesium (Mg) point defect dipole tensor data computed using the GGA-PBE functional. Formation energy E^F is given in eV units, dipole tensor components P_{ij} are also in eV units, and relaxation volume tensor components Ω_{ij} and their trace $\Omega_{\text{rel}} = \Omega_{ii}$ are given in atomic volume units.

Mg_PBE	E^F	P_{11}	P_{22}	P_{33}	P_{12}	P_{23}	P_{31}	Ω_{11}	Ω_{22}	Ω_{33}	Ω_{12}	Ω_{23}	Ω_{31}	Ω_{rel}
Vac	0.840	−1.360	−1.360	−1.785	0.000	0.000	0.000	−0.075	−0.075	−0.137	0.000	0.000	0.000	−0.287
C	2.120	10.499	8.291	9.264	0.621	1.912	1.075	0.775	0.418	0.590	0.201	0.652	0.367	1.782
BO	2.130	11.575	11.575	4.061	0.000	0.000	0.000	0.926	0.926	−0.130	0.000	0.000	0.000	1.723
BS	2.180	14.110	9.742	3.818	0.000	0.000	0.000	1.318	0.610	−0.177	0.000	0.000	0.000	1.751
S	2.230	8.571	8.571	11.064	0.000	0.000	0.000	0.476	0.476	0.842	0.000	0.000	0.000	1.794
O	2.270	8.276	8.276	11.838	0.000	0.000	0.000	0.430	0.430	0.948	0.000	0.000	0.000	1.807

TABLE V. Scandium (Sc) point defect dipole tensor data computed using the GGA-PBE functional. Formation energy E^F is given in eV units, dipole tensor components P_{ij} are also in eV units, and relaxation volume tensor components Ω_{ij} and their trace $\Omega_{\text{rel}} = \Omega_{ii}$ are given in atomic volume units.

Sc_PBE	E^F	P_{11}	P_{22}	P_{33}	P_{12}	P_{23}	P_{31}	Ω_{11}	Ω_{22}	Ω_{33}	Ω_{12}	Ω_{23}	Ω_{31}	Ω_{rel}
Vac	1.910	−2.543	−2.543	−1.761	0.000	0.000	0.000	−0.109	−0.109	−0.053	0.000	0.000	0.000	−0.271
BO	2.060	10.172	10.172	5.712	0.000	0.000	0.000	0.455	0.455	0.116	0.000	0.000	0.000	1.025
O	2.410	9.195	9.195	7.987	0.000	0.000	0.000	0.370	0.370	0.307	0.000	0.000	0.000	1.048
BS	2.560	11.672	9.595	7.323	0.000	0.000	0.000	0.564	0.348	0.218	0.000	0.000	0.000	1.130
C	2.750	7.199	7.014	13.187	0.659	0.199	1.141	0.195	0.175	0.740	0.137	0.044	0.255	1.110
S	2.960	4.214	4.214	16.618	0.000	0.000	0.000	−0.017	−0.017	1.069	0.000	0.000	0.000	1.035

TABLE VI. Yttrium (Y) point defect dipole tensor data computed using the GGA-PBE functional. Formation energy E^F is given in eV units, dipole tensor components P_{ij} are also in eV units, and relaxation volume tensor components Ω_{ij} and their trace $\Omega_{\text{rel}} = \Omega_{ii}$ are given in atomic volume units.

Y_PBE	E^F	P_{11}	P_{22}	P_{33}	P_{12}	P_{23}	P_{31}	Ω_{11}	Ω_{22}	Ω_{33}	Ω_{12}	Ω_{23}	Ω_{31}	Ω_{rel}
Vac	1.860	−3.247	−3.247	−2.035	0.000	0.000	0.000	−0.149	−0.149	−0.044	0.000	0.000	0.000	−0.342
BO	2.080	9.448	9.448	5.579	0.000	0.000	0.000	0.438	0.438	0.105	0.000	0.000	0.000	0.981
O	2.520	8.445	8.445	7.859	0.000	0.000	0.000	0.348	0.348	0.294	0.000	0.000	0.000	0.990
BS	2.520	10.730	8.028	6.467	0.000	0.000	0.000	0.548	0.294	0.169	0.000	0.000	0.000	1.010
C	2.800	6.523	6.043	12.286	1.101	0.416	1.908	0.185	0.139	0.668	0.207	0.081	0.372	0.992
S	2.960	3.138	3.138	15.260	0.000	0.000	0.000	−0.057	−0.057	0.970	0.000	0.000	0.000	0.857

TABLE VII. Lutetium (Lu) point defect dipole tensor data computed using the GGA-PBE functional. Formation energy E^F is given in eV units, dipole tensor components P_{ij} are also in eV units, and relaxation volume tensor components Ω_{ij} and their trace $\Omega_{\text{rel}} = \Omega_{ii}$ are given in atomic volume units.

Lu_PBE	E^F	P_{11}	P_{22}	P_{33}	P_{12}	P_{23}	P_{31}	Ω_{11}	Ω_{22}	Ω_{33}	Ω_{12}	Ω_{23}	Ω_{31}	Ω_{rel}
Vac	1.880	−2.765	−2.765	−1.863	0.000	0.000	0.000	−0.116	−0.116	−0.057	0.000	0.000	0.000	−0.289
BO	2.620	12.130	12.130	6.094	0.000	0.000	0.000	0.535	0.535	0.113	0.000	0.000	0.000	1.183
O	3.090	10.255	10.255	10.617	0.000	0.000	0.000	0.389	0.389	0.450	0.000	0.000	0.000	1.227
BS	3.100	14.979	10.097	7.139	0.000	0.000	0.000	0.758	0.328	0.172	0.000	0.000	0.000	1.258
S	3.600	5.830	5.830	17.760	0.000	0.000	0.000	0.085	0.085	1.015	0.000	0.000	0.000	1.185

TABLE VIII. Titanium (Ti) point defect dipole tensor data computed using the GGA-PBE functional. Formation energy E^F is given in eV units, dipole tensor components P_{ij} are also in eV units, and relaxation volume tensor components Ω_{ij} and their trace $\Omega_{\text{rel}} = \Omega_{ii}$ are given in atomic volume units.

Ti_PBE	E^F	P_{11}	P_{22}	P_{33}	P_{12}	P_{23}	P_{31}	Ω_{11}	Ω_{22}	Ω_{33}	Ω_{12}	Ω_{23}	Ω_{31}	Ω_{rel}
Vac	2.030	−4.057	−4.057	−6.494	0.000	0.000	0.000	−0.067	−0.067	−0.269	0.000	0.000	0.000	−0.403
BO	2.380	13.703	13.703	10.101	0.000	0.000	0.000	0.455	0.455	0.133	0.000	0.000	0.000	1.043
O	2.520	13.722	13.722	11.600	0.000	0.000	0.000	0.427	0.427	0.230	0.000	0.000	0.000	1.084
BS	2.560	10.260	18.562	9.471	0.000	0.000	0.000	0.042	0.959	0.064	0.000	0.000	0.000	1.066
S	2.740	10.028	10.028	18.222	0.000	0.000	0.000	0.124	0.124	0.806	0.000	0.000	0.000	1.054

TABLE IX. Zirconium (Zr) point defect dipole tensor data computed using the GGA-PBE functional. Formation energy E^F is given in eV units, dipole tensor components P_{ij} are also in eV units, and relaxation volume tensor components Ω_{ij} and their trace $\Omega_{\text{rel}} = \Omega_{ii}$ are given in atomic volume units.

Zr_PBE	E^F	P_{11}	P_{22}	P_{33}	P_{12}	P_{23}	P_{31}	Ω_{11}	Ω_{22}	Ω_{33}	Ω_{12}	Ω_{23}	Ω_{31}	Ω_{rel}
Vac	1.940	−5.156	−5.156	−8.022	0.000	0.000	0.000	−0.085	−0.085	−0.267	0.000	0.000	0.000	−0.437
BO	2.690	16.655	16.655	10.344	0.000	0.000	0.000	0.549	0.549	−0.008	0.000	0.000	0.000	1.090
BS	2.820	13.373	22.010	9.137	0.000	0.000	0.000	0.212	1.019	−0.111	0.000	0.000	0.000	1.120
O	2.910	14.795	14.795	16.624	0.000	0.000	0.000	0.357	0.357	0.408	0.000	0.000	0.000	1.122
S	2.990	10.747	10.747	21.872	0.000	0.000	0.000	0.087	0.087	0.844	0.000	0.000	0.000	1.018
C	3.260	12.407	6.929	20.806	0.545	4.744	0.944	0.315	−0.197	0.822	0.102	1.264	0.252	0.939

TABLE X. Hafnium (Hf) point defect dipole tensor data computed using the GGA-PBE functional. Formation energy E^F is given in eV units, dipole tensor components P_{ij} are also in eV units, and relaxation volume tensor components Ω_{ij} and their trace $\Omega_{\text{rel}} = \Omega_{ii}$ are given in atomic volume units.

Hf_PBE	E^F	P_{11}	P_{22}	P_{33}	P_{12}	P_{23}	P_{31}	Ω_{11}	Ω_{22}	Ω_{33}	Ω_{12}	Ω_{23}	Ω_{31}	Ω_{rel}
Vac	2.220	−5.579	−5.579	−7.155	0.000	0.000	0.000	−0.107	−0.107	−0.185	0.000	0.000	0.000	−0.399
BO	3.970	20.247	20.247	12.827	0.000	0.000	0.000	0.544	0.544	0.090	0.000	0.000	0.000	1.178
BS	4.240	17.477	25.345	11.571	0.000	0.000	0.000	0.344	0.853	0.007	0.000	0.000	0.000	1.204
O	4.420	17.467	17.467	21.859	0.000	0.000	0.000	0.342	0.342	0.555	0.000	0.000	0.000	1.239
S	4.580	12.461	12.461	29.710	0.000	0.000	0.000	0.077	0.077	1.021	0.000	0.000	0.000	1.175

TABLE XI. Technetium (Tc) point defect dipole tensor data computed using the GGA-PBE functional. Formation energy E^F is given in eV units, dipole tensor components P_{ij} are also in eV units, and relaxation volume tensor components Ω_{ij} and their trace $\Omega_{\text{rel}} = \Omega_{ii}$ are given in atomic volume units.

Tc_PBE	E^F	P_{11}	P_{22}	P_{33}	P_{12}	P_{23}	P_{31}	Ω_{11}	Ω_{22}	Ω_{33}	Ω_{12}	Ω_{23}	Ω_{31}	Ω_{rel}
Vac	2.670	−8.304	−8.304	−10.825	0.000	0.000	0.000	−0.087	−0.087	−0.164	0.000	0.000	0.000	−0.338
S	4.680	49.584	49.584	47.468	0.000	0.000	0.000	0.630	0.630	0.547	0.000	0.000	0.000	1.808
BO	5.180	53.296	53.296	27.405	0.000	0.000	0.000	0.830	0.830	−0.004	0.000	0.000	0.000	1.657
BS	5.530	56.095	50.360	25.391	0.000	0.000	0.000	0.961	0.723	−0.053	0.000	0.000	0.000	1.631
O	6.070	38.632	38.632	65.968	0.000	0.000	0.000	0.303	0.303	1.153	0.000	0.000	0.000	1.759

TABLE XII. Rhenium (Re) point defect dipole tensor data computed using the GGA-PBE functional. Formation energy E^F is given in eV units, dipole tensor components P_{ij} are also in eV units, and relaxation volume tensor components Ω_{ij} and their trace $\Omega_{\text{rel}} = \Omega_{ii}$ are given in atomic volume units.

Re_PBE	E^F	P_{11}	P_{22}	P_{33}	P_{12}	P_{23}	P_{31}	Ω_{11}	Ω_{22}	Ω_{33}	Ω_{12}	Ω_{23}	Ω_{31}	Ω_{rel}
Vac	3.230	−9.621	−9.621	−13.642	0.000	0.000	0.000	−0.074	−0.074	−0.170	0.000	0.000	0.000	−0.317
S	6.690	70.474	70.474	61.363	0.000	0.000	0.000	0.727	0.727	0.501	0.000	0.000	0.000	1.955
BO	7.470	74.564	74.564	34.232	0.000	0.000	0.000	0.917	0.917	−0.061	0.000	0.000	0.000	1.774
BS	7.870	86.971	62.436	29.242	0.000	0.000	0.000	1.342	0.545	−0.158	0.000	0.000	0.000	1.729
O	8.220	52.784	52.784	89.284	0.000	0.000	0.000	0.335	0.335	1.210	0.000	0.000	0.000	1.880

TABLE XIII. Ruthenium (Ru) point defect dipole tensor data computed using the GGA-PBE functional. Formation energy E^F is given in eV units, dipole tensor components P_{ij} are also in eV units, and relaxation volume tensor components Ω_{ij} and their trace $\Omega_{\text{rel}} = \Omega_{ii}$ are given in atomic volume units.

Ru_PBE	E^F	P_{11}	P_{22}	P_{33}	P_{12}	P_{23}	P_{31}	Ω_{11}	Ω_{22}	Ω_{33}	Ω_{12}	Ω_{23}	Ω_{31}	Ω_{rel}
Vac	2.620	−7.597	−7.597	−9.921	0.000	0.000	0.000	−0.088	−0.088	−0.134	0.000	0.000	0.000	−0.309
BO	8.340	57.737	57.737	35.047	0.000	0.000	0.000	0.866	0.866	0.168	0.000	0.000	0.000	1.899
S	8.440	51.060	51.060	60.534	0.000	0.000	0.000	0.619	0.619	0.773	0.000	0.000	0.000	2.011
O	8.520	50.093	50.093	54.297	0.000	0.000	0.000	0.632	0.632	0.651	0.000	0.000	0.000	1.916
BS	9.020	66.678	45.665	39.992	0.000	0.000	0.000	1.124	0.502	0.288	0.000	0.000	0.000	1.914

TABLE XIV. Osmium (Os) point defect dipole tensor data computed using the GGA-PBE functional. Formation energy E^F is given in eV units, dipole tensor components P_{ij} are also in eV units, and relaxation volume tensor components Ω_{ij} and their trace $\Omega_{\text{rel}} = \Omega_{ii}$ are given in atomic volume units.

Os_PBE	E^F	P_{11}	P_{22}	P_{33}	P_{12}	P_{23}	P_{31}	Ω_{11}	Ω_{22}	Ω_{33}	Ω_{12}	Ω_{23}	Ω_{31}	Ω_{rel}
Vac	2.980	−9.753	−9.753	−12.092	0.000	0.000	0.000	−0.087	−0.087	−0.117	0.000	0.000	0.000	−0.290
BO	11.710	81.164	81.164	50.600	0.000	0.000	0.000	0.902	0.902	0.197	0.000	0.000	0.000	2.002
S	11.760	73.322	73.322	83.759	0.000	0.000	0.000	0.677	0.677	0.769	0.000	0.000	0.000	2.123
O	12.140	69.769	69.769	81.278	0.000	0.000	0.000	0.639	0.639	0.756	0.000	0.000	0.000	2.033
BS	12.710	94.323	64.567	56.727	0.000	0.000	0.000	1.197	0.517	0.305	0.000	0.000	0.000	2.019

TABLE XV. Cobalt (Co) point defect dipole tensor data computed using the GGA-PBE functional. Formation energy E^F is given in eV units, dipole tensor components P_{ij} are also in eV units, and relaxation volume tensor components Ω_{ij} and their trace $\Omega_{\text{rel}} = \Omega_{ii}$ are given in atomic volume units.

Co_PBE	E^F	P_{11}	P_{22}	P_{33}	P_{12}	P_{23}	P_{31}	Ω_{11}	Ω_{22}	Ω_{33}	Ω_{12}	Ω_{23}	Ω_{31}	Ω_{rel}
Vac	1.930	−4.697	−4.697	−3.715	0.000	0.000	0.000	−0.119	−0.119	−0.068	0.000	0.000	0.000	−0.305
S	4.310	24.955	24.955	31.679	0.000	0.000	0.000	0.529	0.529	0.836	0.000	0.000	0.000	1.893
BO	4.430	32.672	32.672	15.411	0.000	0.000	0.000	0.913	0.913	0.059	0.000	0.000	0.000	1.884
BS	4.960	39.095	29.016	14.730	0.000	0.000	0.000	1.350	0.576	0.008	0.000	0.000	0.000	1.934
O	5.040	22.934	22.934	39.569	0.000	0.000	0.000	0.397	0.397	1.183	0.000	0.000	0.000	1.978

TABLE XVI. Zinc (Zn) point defect dipole tensor data computed using the GGA-PBE functional. Formation energy E^F is given in eV units, dipole tensor components P_{ij} are also in eV units, and relaxation volume tensor components Ω_{ij} and their trace $\Omega_{\text{rel}} = \Omega_{ii}$ are given in atomic volume units.

Zn_PBE	E^F	P_{11}	P_{22}	P_{33}	P_{12}	P_{23}	P_{31}	Ω_{11}	Ω_{22}	Ω_{33}	Ω_{12}	Ω_{23}	Ω_{31}	Ω_{rel}
Vac	0.310	−3.855	−3.855	0.991	0.000	0.000	0.000	−0.295	−0.295	0.498	0.000	0.000	0.000	−0.092
O	1.240	6.875	6.875	13.702	0.000	0.000	0.000	−0.089	−0.089	2.098	0.000	0.000	0.000	1.919
C	1.250	6.843	6.195	13.859	−0.467	0.561	−0.808	−0.095	−0.143	2.156	−0.069	0.185	−0.267	1.918
S	1.370	6.278	6.278	14.999	0.000	0.000	0.000	−0.180	−0.180	2.395	0.000	0.000	0.000	2.035
BO	2.970	19.986	19.986	6.317	0.000	0.000	0.000	1.073	1.073	−0.370	0.000	0.000	0.000	1.776
BS	3.070	30.173	12.273	6.529	0.000	0.000	0.000	1.810	0.483	−0.427	0.000	0.000	0.000	1.866

TABLE XVII. Zinc (Zn) point defect dipole tensor data computed using the GGA-PBE functional. Formation energy E^F is given in eV units, dipole tensor components P_{ij} are also in eV units, and relaxation volume tensor components Ω_{ij} and their trace $\Omega_{\rm rel} = \Omega_{ii}$ are given in atomic volume units.

Zn_PBEsol	E^F	P_{11}	P_{22}	P_{33}	P_{12}	P_{23}	P_{31}	Ω_{11}	Ω_{22}	Ω_{33}	Ω_{12}	Ω_{23}	Ω_{31}	$\Omega_{\rm rel}$
Vac	0.390	−2.556	−2.556	−3.263	0.000	0.000	0.000	−0.062	−0.062	−0.263	0.000	0.000	0.000	−0.387
O	1.460	5.342	5.342	24.263	0.000	0.000	0.000	−0.205	−0.205	2.478	0.000	0.000	0.000	2.067
S	1.660	5.109	5.109	25.349	0.000	0.000	0.000	−0.237	−0.237	2.607	0.000	0.000	0.000	2.132
BO	3.310	17.911	17.911	15.845	0.000	0.000	0.000	0.569	0.569	1.064	0.000	0.000	0.000	2.203
C	3.360	7.439	6.714	32.371	−0.594	0.628	−1.028	−0.255	−0.298	3.307	−0.071	0.119	−0.195	2.755
BS	3.440	29.113	9.791	15.081	0.000	0.000	0.000	1.236	0.082	0.921	0.000	0.000	0.000	2.239

mesh density, or choice of Be pseudopotential. Here we used $E_{\rm cut} = 800\,{\rm eV}$ compared to $E_{\rm cut} = 1.4\times{\rm ENMAX} = 345\,{\rm eV}$ where ENMAX is the recommended cutoff supplied in the Be POTCAR file, or 432 eV for the Be_sv POTCAR.

The relaxation volume tensor of a vacancy in an hcp crystal has the form [38]

$$\mathbf{\Omega}^{\rm Vac} = \begin{pmatrix} \Omega_a^{\rm Vac} & 0 & 0 \\ 0 & \Omega_a^{\rm Vac} & 0 \\ 0 & 0 & \Omega_c^{\rm Vac} \end{pmatrix}, \tag{12}$$

for independent strains in the basal plane $\Omega_a^{\rm Vac}$ and along the c axis $\Omega_c^{\rm Vac}$. $\Omega_a^{\rm Vac}$ and $\Omega_c^{\rm Vac}$ are plotted in Fig. 7 as a function of c/a ratio. For elements with the less than ideal c/a ratio, we observe a weak positive correlation. The extrapolated values of $\Omega_c^{\rm Vac}$ for Be, Zn, and Cd indicate expansion along [0001], despite the fact that, in general, vacancies in materials are centers of contraction. However, we note that accurately simulating group XII metals using DFT is challenging due to their fully occupied d and s shells; see Table I. As a result, the conventional notion of chemical bonding involving the hybridization of atomic electronic orbitals and formation of collective bonding and antibonding states, typical of elements with partially filled atomic orbitals [72], clearly does not apply here, highlighting the particularly significant part played by the electron exchange and correlation effects [73]. Thus, we often found that the results were extremely sensitive to the choice of exchange-correlation functional and the choice of the k-point mesh, and at times the results did not converge satisfactorily with respect to cell size. When relaxed under zero stress, some of the larger supercells containing a vacancy expanded along the c axis while others exhibited anisotropic contraction in all directions. In general, coupled cluster calculations that appear able to capture the exchange-correlation effects in these metals more accurately [73] are required to ascertain the nature of deformations induced by vacancies in Zn and Cd.

In general, a second rank tensor $\mathbf{\Omega}$ may be decomposed into an isotropic $\frac{1}{3}{\rm Tr}(\mathbf{\Omega})\mathbf{I}$ and deviatoric $\mathbf{\Omega}^d = \mathbf{\Omega} - \frac{1}{3}{\rm Tr}(\mathbf{\Omega})\mathbf{I}$ parts, where $\mathbf{I}$ is the Kronecker delta tensor. Hence, we may rewrite Eq. (12) as

$$\mathbf{\Omega}^{\rm Vac} = \frac{\Omega_{ii}^{\rm Vac}}{3}\mathbf{I} + \frac{\Omega_c^{\rm Vac} - \Omega_a^{\rm Vac}}{3}\begin{pmatrix} -1 & 0 & 0 \\ 0 & -1 & 0 \\ 0 & 0 & 2 \end{pmatrix}, \tag{13}$$

where the relaxation volume $\Omega_{ii}^{\rm Vac}$ is the trace of tensor $\mathbf{\Omega}^{\rm Vac}$, and the principal shear strain $\Omega_c^{\rm Vac} - \Omega_a^{\rm Vac}$ is a measure of the difference in the c and a strains induced by a vacancy, and is proportional to the magnitude of the deviatoric part of $\mathbf{\Omega}^{\rm Vac}$. The volumetric and shear strains are plotted in Fig. 8 with respect to the group number of the element in the Periodic Table. The dilatation and shear strains become more negative in elements of group IV, increasing again across a given period. Once again, the cases of Cd and Zn are anomalous, with the $\Omega_c - \Omega_a$ value being relatively large due to the substantial positive c strain.

B. Self-interstitial atoms

In Fig. 9, we tabulate the formation energies of SIA configurations in hcp metals across the Periodic Table. The lowest formation energy SIA, $E^F_{\rm min}({\rm SIA})$, is highlighted in boldface and a white border and represents the most stable configuration at zero kelvin. The entries to the table are colored according to the positive energy difference $E^F({\rm SIA}) - E^F_{\rm min}({\rm SIA})$. For certain metals, such as Mg, the formation energies of multiple configurations are similar to $E^F_{\rm min}({\rm SIA})$ and thus it is difficult to determine the ensemble

TABLE XVIII. Cadmium (Cd) point defect dipole tensor data computed using the GGA-PBE functional. Formation energy E^F is given in eV units, dipole tensor components P_{ij} are also in eV units, and relaxation volume tensor components Ω_{ij} and their trace $\Omega_{\rm rel} = \Omega_{ii}$ are given in atomic volume units.

Cd_PBE	E^F	P_{11}	P_{22}	P_{33}	P_{12}	P_{23}	P_{31}	Ω_{11}	Ω_{22}	Ω_{33}	Ω_{12}	Ω_{23}	Ω_{31}	$\Omega_{\rm rel}$
Vac	0.100	−4.338	−4.338	−0.346	0.000	0.000	0.000	−0.403	−0.403	0.531	0.000	0.000	0.000	−0.274
C	0.930	9.658	8.525	11.521	0.347	0.981	0.600	0.184	−0.051	1.792	0.144	1.185	0.725	1.926
O	0.960	9.247	9.247	11.648	0.000	0.000	0.000	0.073	0.073	1.804	0.000	0.000	0.000	1.950
S	1.030	9.054	9.054	12.606	0.000	0.000	0.000	−0.015	−0.015	2.090	0.000	0.000	0.000	2.060
BS	1.730	34.434	11.081	8.480	0.000	0.000	0.000	4.053	−0.789	−0.993	0.000	0.000	0.000	2.272
BO	2.150	21.451	21.451	6.373	0.000	0.000	0.000	1.655	1.655	−1.372	0.000	0.000	0.000	1.939

TABLE XIX. Cadmium (Cd) point defect dipole tensor data computed using the GGA-PBE functional. Formation energy E^F is given in eV units, dipole tensor components P_{ij} are also in eV units, and relaxation volume tensor components Ω_{ij} and their trace $\Omega_{\rm rel} = \Omega_{ii}$ are given in atomic volume units.

Cd_PBEsol	E^F	P_{11}	P_{22}	P_{33}	P_{12}	P_{23}	P_{31}	Ω_{11}	Ω_{22}	Ω_{33}	Ω_{12}	Ω_{23}	Ω_{31}	$\Omega_{\rm rel}$
Vac	0.210	−4.719	−4.719	0.706	0.000	0.000	0.000	−0.308	−0.308	0.428	0.000	0.000	0.000	−0.188
O	1.310	9.835	9.835	16.713	0.000	0.000	0.000	0.022	0.022	1.849	0.000	0.000	0.000	1.894
S	1.470	9.479	9.479	17.856	0.000	0.000	0.000	−0.038	−0.038	2.046	0.000	0.000	0.000	1.970
C	2.750	15.503	16.578	30.941	−0.227	−0.931	−0.393	−0.137	−0.041	3.571	−0.040	−0.427	−0.180	3.393
BO	2.760	24.471	24.471	7.861	0.000	0.000	0.000	1.203	1.203	−0.481	0.000	0.000	0.000	1.925
BS	2.800	36.101	17.001	8.341	0.000	0.000	0.000	2.161	0.463	−0.550	0.000	0.000	0.000	2.073

of SIA defects at elevated temperatures within the uncertainties of density functional theory calculation. In particular, at nonzero temperatures SIAs migrate and transform into different configurations at rates determined by the energy barriers between configurations, even if the SIAs have not reacted with other defect species instead. Typically, SIA migration barriers are low [74] and thus, while we have not evaluated these barriers in this study, we may estimate them via examining the differences in formation energy between different configurations. SIA formation energies tend to increase towards group VIII, as shown in Fig. 10 where the minimum formation energy is plotted with respect to the group number. Our values for E_F are broadly in agreement with other DFT calculations for Be [12,20,21], Mg [12,39], Y [22], Ti [12,13], Zr [13], Hf [13], Co [12], Zn [12,19], and Cd [12]. For half of the metals with a less than ideal c/a ratio, the lowest-energy SIA configuration is the basal octahedral SIA. In other elements, BO is often close to the lowest-energy SIA configuration. In particular, $E^F(\mathrm{BO}) - E^F_{\rm min}(\mathrm{SIA}) \lesssim 0.1$ eV for Mg, Ru, Os, Co, and Tl.

Crowdion configurations of SIA defects in hcp elements are often unstable and have high formation energies. The linear structure of a crowdion in some bcc metals, like Cr, Mo, and W, renders it mechanically unstable against buckling [7]. Such instabilities have also been observed in simulations of crowdion defects in group IV hcp metals Ti, Zr, and Hf [13].

The formation energy differences $E^F(\mathrm{BS}) - E^F(\mathrm{BO})$ across group III and IV metals are small. Vérité *et al.* [13] proposed that in group IV elements, SIA defects migrate through a process involving a jump from BO to a buckled crowdion or rotated split dumbbell that then glides along the c axis before hopping to another BO configuration. $E^F(\mathrm{S}) - E^F(\mathrm{BO})$ is higher for group III elements compared to elements of group IV and thus a BO SIA can migrate within the basal plane by alternating with BS configurations, as suggested for one of the possible migration pathways in Zr [36].

For the group III metals Sc and Y, and the lanthanide Lu, resistivity recovery experiments have shown the onset of stage I_D recovery to be at temperatures T_{1D} between 105 and 130 K ([75], S2.4). This corresponds to migration energies of $\sim$0.3 eV and, within the uncertainties of the simulation and experiment, it is not clear whether this is consistent with the lowest formation energy difference of $\sim 0.4 - 0.5$ eV found in our simulation.

Our calculations suggest that the most stable SIA in Mg adopts the crowdion configuration. However, the difference between the formation energy of a crowdion and any other SIA configuration is less than 0.2 eV. Therefore, it is difficult to determine the lowest-energy SIA with complete certainty, and to verify predictions against experimental information. Otherwise, we observe that the similarity of formation energies implies that the hcp crystal lattice of Mg is essentially indifferent to the configuration adopted by an extra atom. Furthermore, this also implies that the SIA migration is isotropic. A similar picture of SIA migration emerges in thallium where, with the exception of a crowdion, the formation energies of all the SIA configurations are the same within 0.12 eV.

Tc and Re in group VII have a lower than ideal c/a ratio and yet, despite this, the basal octahedral SIA has a large formation energy. This marks group VII as an anomaly among all of the low c/a ratio hcp metals where BO is otherwise a low-energy, if not the most stable configuration. The just over half-full d band in hcp Tc and Re leads to high cohesive energies and low compressibility [72]. Thus the group VII metals are expected to exhibit bonding properties that are qualitatively different from other transition metals. The high-energy BO, BS, and O configurations, together with an unstable crowdion structure, imply that SIAs migrate through the rotation of low-symmetry dumbbells or buckled crowdions

TABLE XX. Thallium (Tl) point defect dipole tensor data computed using the GGA-PBE functional. Formation energy E^F is given in eV units, dipole tensor components P_{ij} are also in eV units, and relaxation volume tensor components Ω_{ij} and their trace $\Omega_{\rm rel} = \Omega_{ii}$ are given in atomic volume units.

Tl_PBE	E^F	P_{11}	P_{22}	P_{33}	P_{12}	P_{23}	P_{31}	Ω_{11}	Ω_{22}	Ω_{33}	Ω_{12}	Ω_{23}	Ω_{31}	$\Omega_{\rm rel}$
Vac	0.410	−2.194	−2.194	−2.286	0.000	0.000	0.000	−0.164	−0.164	−0.104	0.000	0.000	0.000	−0.431
S	0.920	8.164	8.164	11.583	0.000	0.000	0.000	0.465	0.465	0.803	0.000	0.000	0.000	1.734
O	0.930	7.884	7.884	11.923	0.000	0.000	0.000	0.415	0.415	0.875	0.000	0.000	0.000	1.705
BO	0.990	8.153	8.153	9.646	0.000	0.000	0.000	0.554	0.554	0.543	0.000	0.000	0.000	1.651
BS	1.000	9.680	7.287	8.770	0.000	0.000	0.000	1.340	−0.069	0.394	0.000	0.000	0.000	1.665

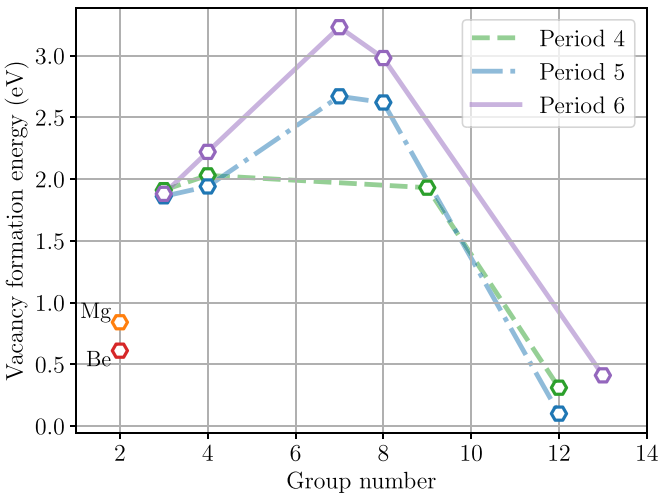


FIG. 6. Formation energies of vacancies in hcp metals plotted as a function of the group number of the respective chemical element in the Periodic Table.

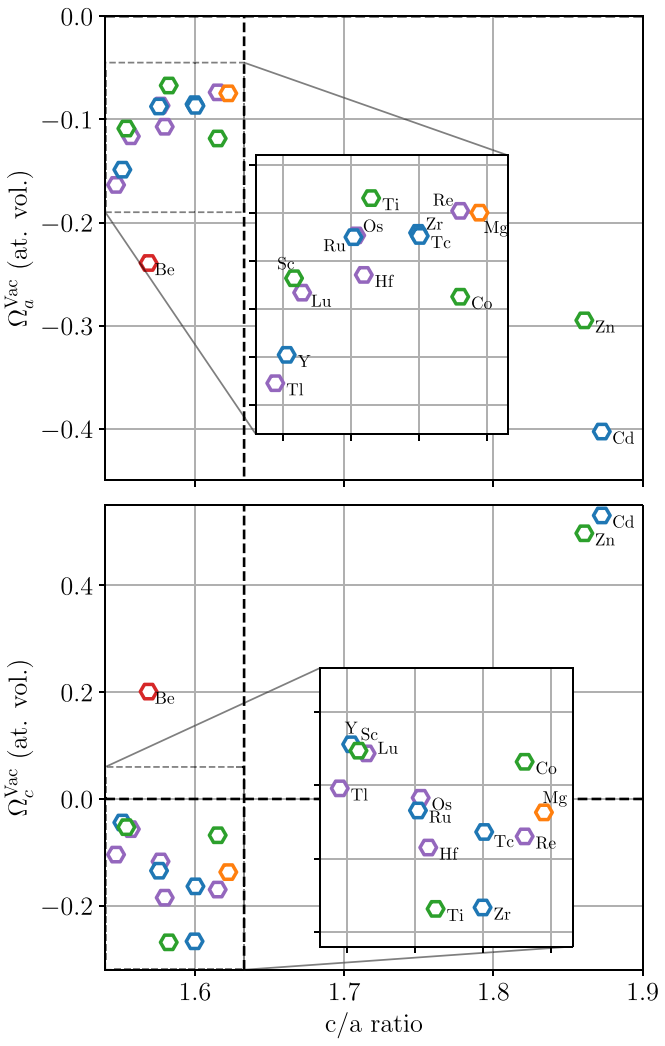


FIG. 7. Vacancy relaxation volume tensor components Ω_a and Ω_c, defined in Eq. (12) with respect to the hcp crystallographic coordinate system. Vertical dashed lines indicate the ideal ratio $c/a = \sqrt{8/3}$.

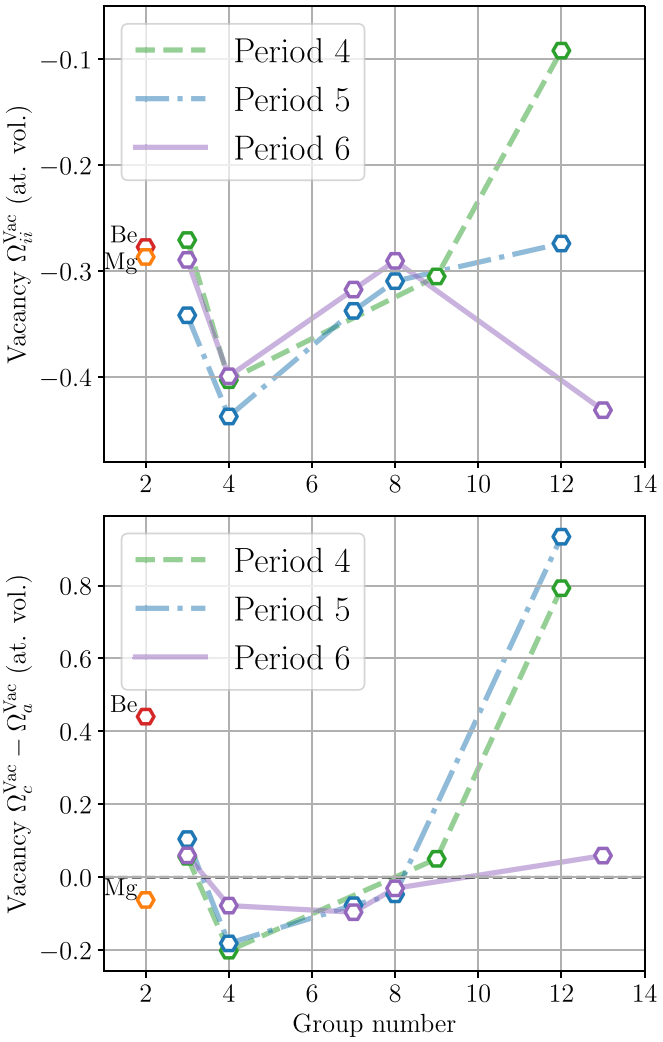


FIG. 8. Vacancy relaxation volume tensor components Ω_a and Ω_c, defined in Eq. (12) with respect to the hcp crystallographic coordinate system. Vertical dashed lines indicate the ideal ratio $c/a = \sqrt{8/3}$.

as described by Vérité *et al.* [13]. Understandably, there is little experimental information available on the radioactive element Tc. For the remaining group VII hcp metal, Re, the SIA migration enthalpy of 0.16 eV has been measured experimentally [75]. This differs significantly from our lowest value $E^F(\text{SIA}) - E^F_{\text{min}}(\text{SIA})$ value of 0.89 eV. The existence of a lower-symmetry rotated dumbbell that has the formation energy close to that of S is possible, or the observed low migration energy may be associated with impurities and imperfections in the Re sample.

To the best of our knowledge, no experimental information on point defect properties in elements of group VIII is available. Our data suggest that $E^F(\text{BS})$ has a high formation energy relative to the lowest-energy configurations. This raises the possibility that SIAs transform between BO, O and S configurations with relative ease, biasing SIA migration along the c axis.

Magnetism in Co does not appear to produce any anomalies in the ordering of SIA formation energies. Given the lower

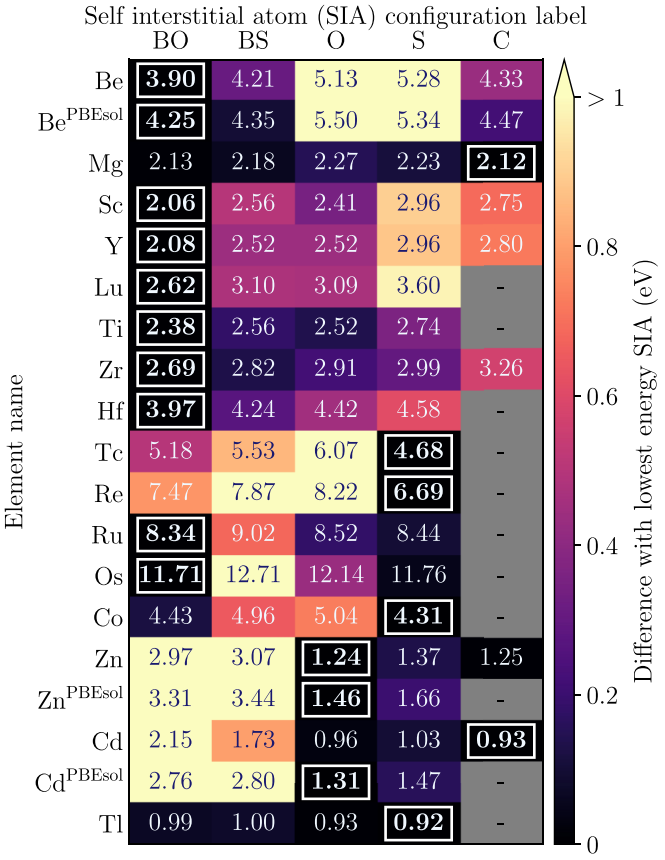


FIG. 9. Table of SIA formation energies across the hcp elements in the Periodic Table. For a given element, cells are colored according to the difference between the formation energy of a configuration and the energy of the most stable SIA structure, highlighted in boldface and white borders. Calculations performed using the PBEsol exchange-correlation functional are indicated by a superscript for Be, Zn, and Cd.

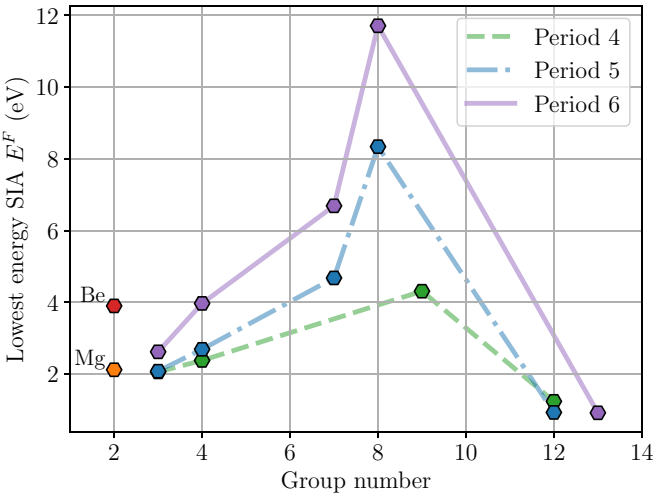


FIG. 10. The lowest self-interstitial atom defect formation energy in hcp elements with respect to the group number in the Periodic Table.

than ideal c/a ratio of cobalt, the formation energy of the BO configuration is still low.

Zn and Cd exhibit relatively high formation energies for the basal plane SIAs, whereas the E_F values for O, S and C configurations are similar. Tracer diffusion experiments have indicated that the [0001] split dumbbell is the most stable SIA configuration in both hcp group XII metals [76], consistent with the low formation energy of the S configuration found in this study. This implies that the diffusion of SIAs occurs rapidly along the c axis and relatively slow in the basal plane. There is a great deal of uncertainty in modeling Zn and Cd using DFT as many exchange-correlation functionals are unable to describe correlations in the d-electron shell with sufficient accuracy [73]. Furthermore, we found that even the predicted lattice parameters and elastic constants of Zn and Cd are highly sensitive to the k-point mesh employed. We repeated our calculations for Cd with the PBEsol E_{xc} functional [59], finding that the crowdion defect relaxed into a high-energy nonlinear structure and the lowest formation energy configuration was instead an octahedral SIA. However, the energy of the basal configuration remained significantly higher than that for the inter-basal plane SIAs.

In Fig. 11 we show (0001) cross sections of electron charge density difference (ECDD) for the basal octahedral SIAs in Be, Mg, Zr, Re, Zn, and Tl. Despite belonging to the same group, Be and Mg exhibit very different bonding characters that are highly anisotropic and isotropic respectively. The d-orbital bonding is apparent for Zr and Re whereas the ellipsoidal regions of charge depletion in Zn arise from the completed d shell. A greater degree of anisotropy in the bonding re-emerges in Tl due to the valence p electrons. While the ECDD maps are consistent with the expected bonding in these metals, they do not immediately provide an explanation for the relative stability of different SIA configurations. We note that a similar lack of direct correspondence between the type of interatomic bonding and the structure of defects was found in bcc metals [2].

The relaxation volumes and magnitude of deviatoric tensors for the lowest formation energy interstitials computed for various chemical elements are plotted in Fig. 12. In a given group, the relaxation volume increases from period 4 to period 6 with the exception of elements of group III. Across a given period, the relaxation volume peaks at group VIII. With the exception of group XII, the magnitudes of deviatoric tensors across the hcp transition metals are similar.

Huang diffuse x-ray scattering experiments provide information about the invariants of dipole tensors of low-energy SIAs. In particular, the anisotropy ratio P_{33}/P_a is often reported for hcp metals [12,77] where

$$P_a = \sqrt{\left[2\left(P_{11}^2 + P_{22}^2 + 2P_{12}^2\right) + (P_{11} + P_{22})^2\right]/8}. \quad (14)$$

Values of P_{33}/P_a for the lowest formation energy SIA configurations are plotted in Fig. 13 as a function of the group number. There is a positive linear correlation along the d block. However, we caution that the anisotropy ratio varies strongly as a function of defect configuration and thus, particularly where there is uncertainty as to the true lowest-energy SIA, different exchange-correlation functionals may produce qualitatively different trends. No discernible trend could be identified with respect to the c/a ratio of a given metal.

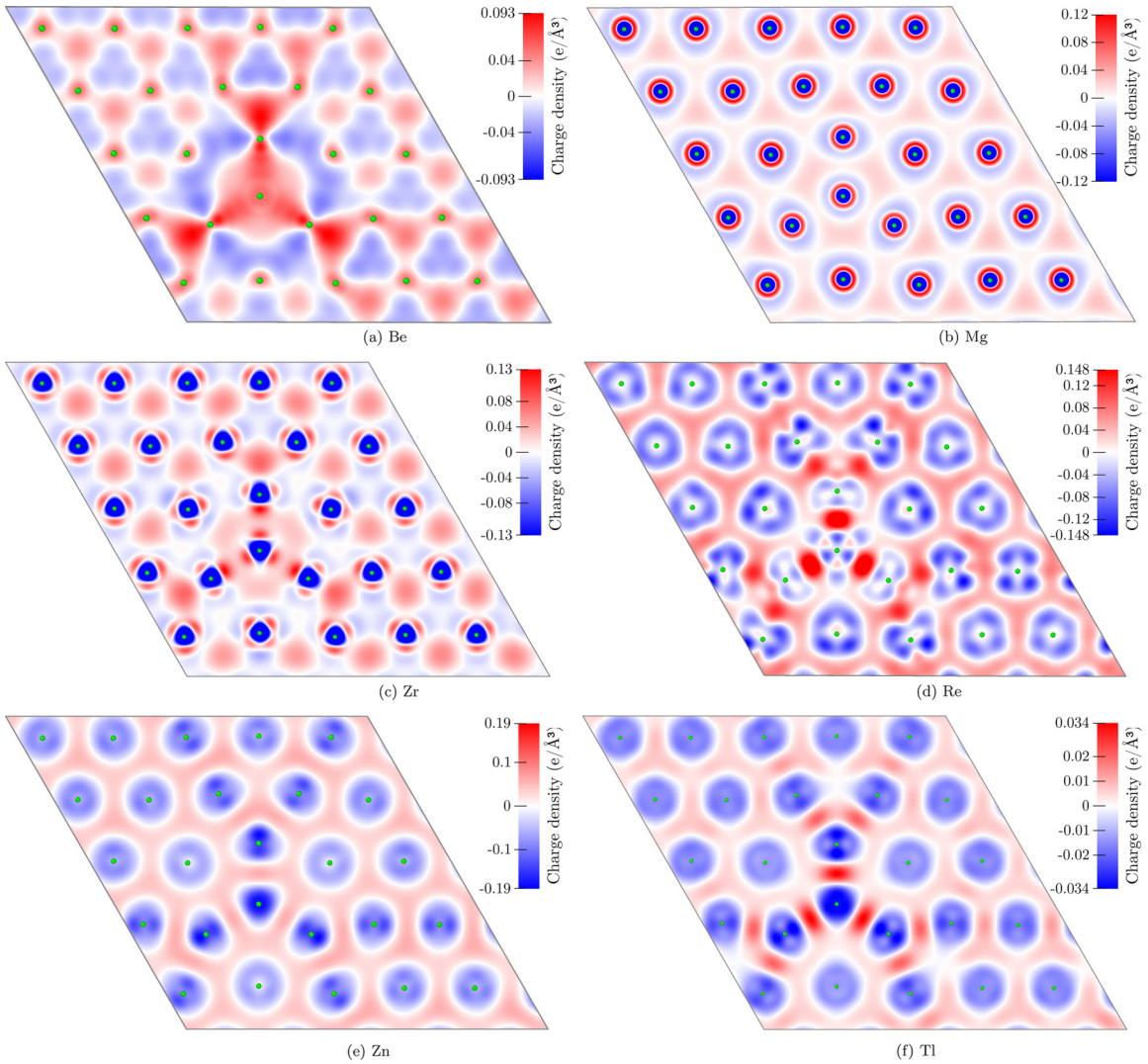


FIG. 11. Electron charge density difference (ECDD) of a relaxed basal octahedral (BO) self interstitial atom (SIA) defect in (a) Be, (b) Mg, (c) Zr, (d) Re, (e) Zn, and (f) Tl. ECDD is defined as the fully convergent electron density derived from *ab initio* simulations minus the superposition of atomic charge densities. All renders show a (0001) cross section of the ECDD containing the BO SIA. The positions of atomic nuclei within the slice are rendered as green spheres.

IV. HCP, BCC, AND FCC METALS

All the new data on point defect relaxation volumes computed for hcp metals have now been combined with the data on bcc [2] and fcc [3] data to provide a comprehensive review of properties of defects across the Periodic Table. We compare results obtained using the PBE functional across all the datasets for consistency, and owing to the fact that it was predominantly the PBE functional that was employed across all the elements.

The formation energies of vacancies and lowest-energy SIAs are plotted in Fig. 14. The formation energy E^F increases towards the middle of the transition metal block for both types of point defects, with slight variation in the location of the peak between the periods and point defect types. Across the third period, vacancy and SIA formation energies are maximum at antiferromagnetic Cr in group VI. The largest vacancy formation energy is also at group VI for Mo and W in periods 4 and 5, respectively. For the self-interstitial atom defects, E^F(SIA) instead drops substantially at group VII for Tc and Re, most likely due to their close to half-full d band, before rising slightly at Ru and Os in group VIII.

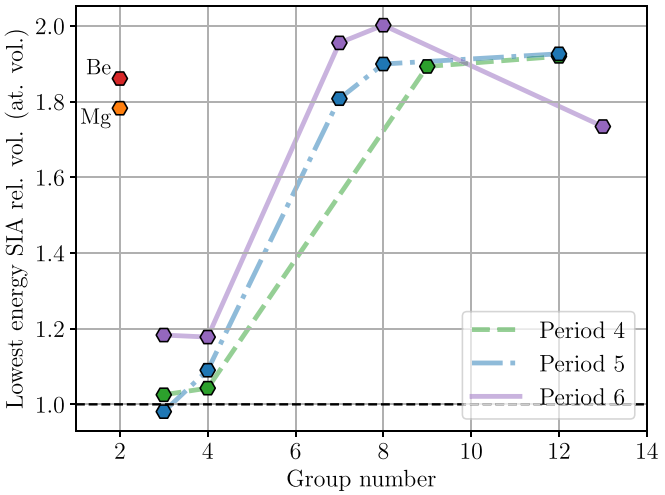
The equilibrium concentration c_D of defects of type D at a constant external stress σ_{ij} and temperature T is given by

$$c_\mathrm{D} = e^{-G^F(\mathrm{D})/k_B T}, \tag{15}$$

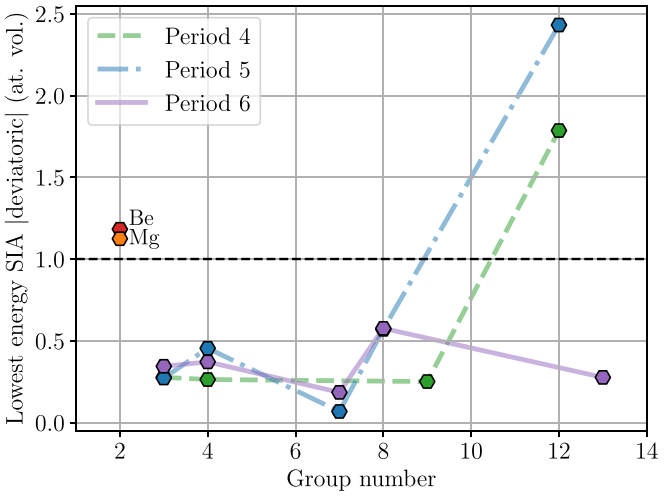
where k_B is Boltzmann's constant, and the Gibbs formation free energy,

$$G^F(\mathrm{D}) = E^F(D) + \sigma_{ij}\Omega^F_{ij}(\mathrm{D}) - S^F(\mathrm{D})T, \tag{16}$$

is a sum of the formation energy $E^F(\mathrm{D})$; formation volume $\Omega^F_{ij}(\mathrm{D}) = \Omega_{ij}(\mathrm{D}) \pm \frac{1}{3}\Omega\delta_{ij}$ multiplied by stress, for relaxation volume $\Omega_{ij}(\mathrm{D})$ and atomic volume Ω; and formation entropy $S^F(\mathrm{D})$ [78]. In the definition of $\Omega^F_{ij}(\mathrm{D})$ the plus sign refers to a vacancy, making the vacancy formation volume a positive quantity [79], whereas the minus sign refers to a self-interstitial atom defect.



(a)



(b)

FIG. 12. Relaxation volumes and the magnitude of relaxation volume deviatoric tensor for the lowest-energy SIA defect for each element shown in Fig. 9.

Often, the large formation energies of SIAs render their thermal equilibrium population negligible compared to vacancies, whose concentrations at high homologous temperatures are in the range $10^{-3} - 10^{-2}$ per lattice site [79]. However, this study shows that in some metals, the vacancy formation energy and the lowest SIA formation energy are fairly close, differing by less than 20% for Sc and Y. This is illustrated in Fig. 15 where the ratio $E^F(\text{Vac})/E^F_{\text{min}}(\text{SIA})$ is plotted against the group number across the hcp, bcc, and fcc metals. Compared to vacancies, SIAs require more energy to be created with increasing group number across the transition metals. The melting points of Sc and Y are in excess of 1500 K [80] and thus, assuming that the formation energies do not change appreciably across the hcp to bcc phase transition, the formation energy contribution to the concentration of SIAs at thermal equilibrium is expected to be similar to that of vacancies. At high homologous temperatures, the formation entropy of defects in metals stems primarily from thermal

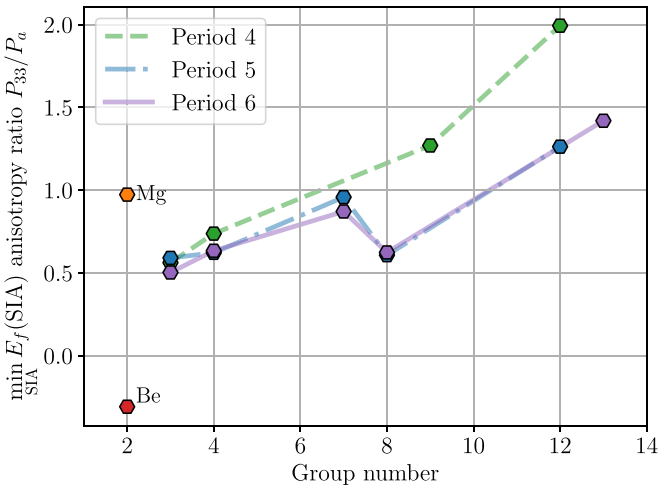


FIG. 13. Plot of dipole tensor anisotropy ratio for the lowest-energy SIA as a function of the Periodic Table group number for a given element. The definition of P_a is given in Eq. (14) of the main text.

vibrations [81]:

$$S^F_{\text{vib}}(\text{D}) = k_B \ln\left(\frac{\prod_{\nu_B}(\hbar\omega_{\nu_B})^{\frac{N_B \pm N_D}{N_B}}}{\prod_{\nu_D}\hbar\omega_{\nu_D}}\right). \tag{17}$$

Here, N_B and N_D are the number of bulk atoms and point defects, respectively, and the phonon frequencies of the bulk ω_{ν_B} and defect ω_{ν_D} systems are computed via computing eigenvalues of the Hessian. The vibrational formation entropies of point defects in metals are on the order of $4k_B$ [82,83]. However, the well known low migration energy of SIAs in pure elemental metals suggests that the lowest-frequency phonon mode for a SIAs is likely low, and this may significantly increase the thermal equilibrium concentration of SIAs. Furthermore, the stochastic nearly free motion of SIAs provides an additional contribution to the formation entropy that is yet to be determined satisfactorily and may be substantial. Hence, we postulate that appreciable concentrations of SIAs may be produced and observed close to the melting point in metals such as Sc and Y.

These trends with respect to changes in the electronic structure of metals are somewhat similar to the variation of their bulk moduli. In particular, Fig. 16 shows that metals become stiffer towards the middle of the transition block. Conversely, the atomic volume is also minimum at that point.

Figure 17 illustrates the occurrence of a strong correlation between the relaxation volume of a defect and the atomic volume of the respective element. The relaxation volume of a point defect vacancies Ω^{Vac} and the most stable SIAs Ω^{SIA} are well approximated by

$$\Omega^{\text{Vac}} \sim -0.35\Omega, \tag{18}$$

$$\Omega^{\text{SIA}} \sim +1.46\Omega, \tag{19}$$

where Ω is the atomic volume. The coefficient of determination R^2 for both linear fits is 0.93.

Equations (19) suggest that Ω^{Vac} and Ω^{SIA} follow the same inverted parabolic profile of Ω with respect to group number

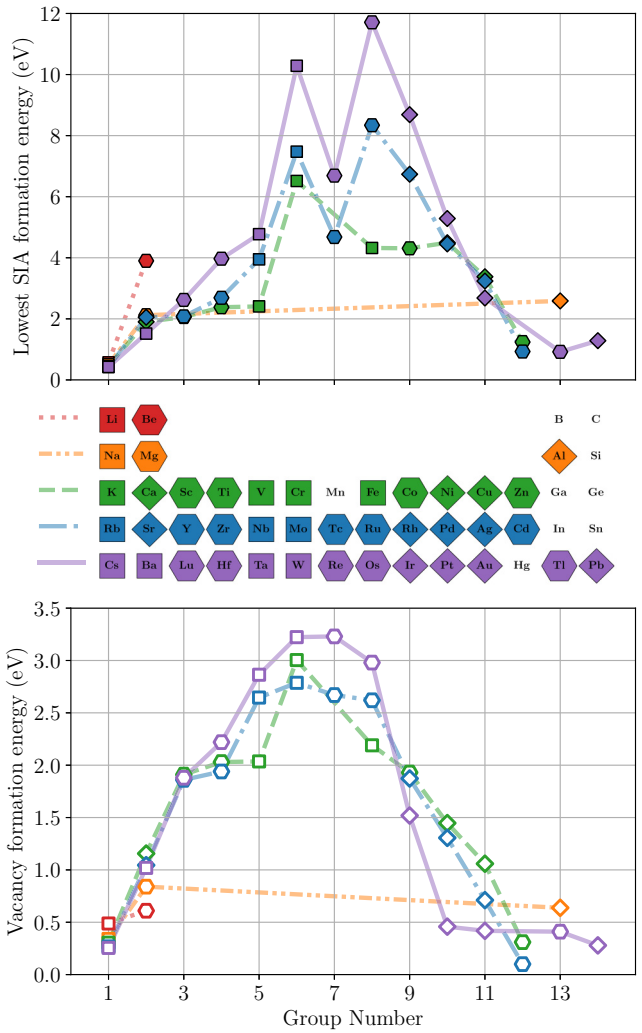


FIG. 14. Point defect formation energies for SIAs (top) and vacancies (bottom) as a function of group number in the Periodic Table for all the bcc [2], fcc [3], and hcp (this work) elements. Data for fcc Th have been excluded and hcp Lu was treated as a group III element. Lines connect elements of the same period, as shown to the left of the Periodic Table at the center of the figure.

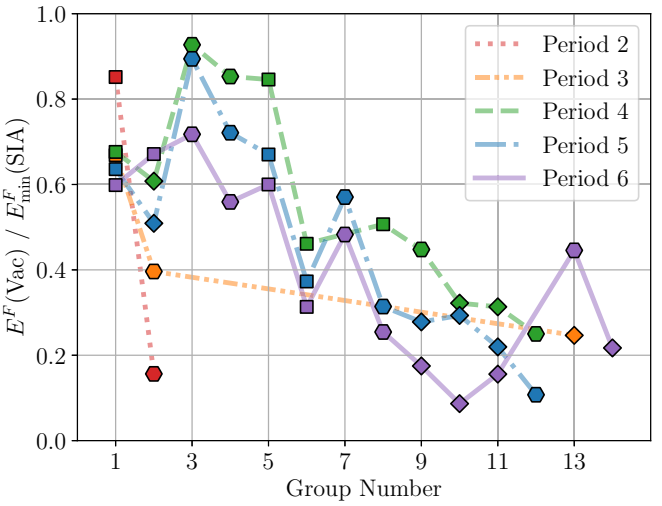


FIG. 15. Ratio of vacancy formation energy E^F(Vac) to the lowest self-interstitial atom formation energy $E^F_{\min}$(SIA) as a function of group number in the Periodic Table for all the bcc, fcc, and hcp elements.

shown in Fig. 16. As the atomic number increases down groups I and II, the atomic volume expands as a result of accumulation of a greater number of complete shells [72] whereas the increased nuclear charge contracts the nearest neighbor distances from group I to II. The parabolic variation across the transition metal periods is influenced primarily by the d-bond energy contribution [72], suggesting that d-bonding effects are similarly responsible for the observed trends in the defect energies. sd-hybridization effects also likely play a part, particularly in the noble metals and, as discussed in the previous section, the full d and s shells of Zn and Cd elevate the importance of electron exchange and correlation effects, rendering these elements anomalous among the transition metals. Period 3 shows marked differences from the $4d$ and $5d$ series due to the pronounced effect of magnetism, arising from the relatively localized $3d$ orbitals [84]. The p valence electrons in group XIII and XIV metals Al, Tl, and Pb lead to stronger bonding and thus relatively small nearest neighbor distances.

The trace of the dipole tensor exhibits a correlation with the bulk modulus, although this correlation is weaker than the correlation between the relaxation volume and atomic volume noted above. This is illustrated in Fig. 18 such that

$$P_{ii}^{\mathrm{Vac}}\ (\mathrm{eV}) \sim -0.10B\ (\mathrm{GPa}), \tag{20}$$

$$P_{ii}^{\mathrm{SIA}}\ (\mathrm{eV}) \sim +0.49B\ (\mathrm{GPa}), \tag{21}$$

where proportionality coefficients are in units of eV/GPa. The coefficients of determination R^2 are 0.79 and 0.92, for vacancies and SIAs, respectively. This correlation suggests that the first invariant of the point defect dipole tensors follows a similar parabola profile as the bulk moduli with respect to the group number, as shown in Fig. 16. Similar to the discussion on atomic volumes, the d-bond energy in the transition metals is responsible for the parabolic variation in bulk modulus with increasing number of d-shell electrons [72].

The Voigt averaged bulk modulus B often provides a good approximation for the pressure $p = -\frac{1}{3}\sigma_{ii}$ and stress tensor σ_{ij} arising from dilatation Δ such that

$$p = B\Delta, \tag{22}$$

where Eq. (22) is exact for cubic metals. Therefore, from Eq. (19) it follows that the trace of the dipole tensor, P_{ii}, for either vacancies or SIAs is expected to scale linearly with the bulk modulus, according to

$$P_{ii} \sim 3B\Omega. \tag{23}$$

Thus, one of the correlations indicated by Eqs. (19) and (21) suggests the other. However, due to the fact that Eq. (22) does not hold for hcp metals, the optimally fitted correlation coefficients are not related exactly by the relation expressed by Eq. (23).

In Fig. 19, vacancy and SIA relaxation volumes, in units of atomic volume, are plotted as functions of the element's group

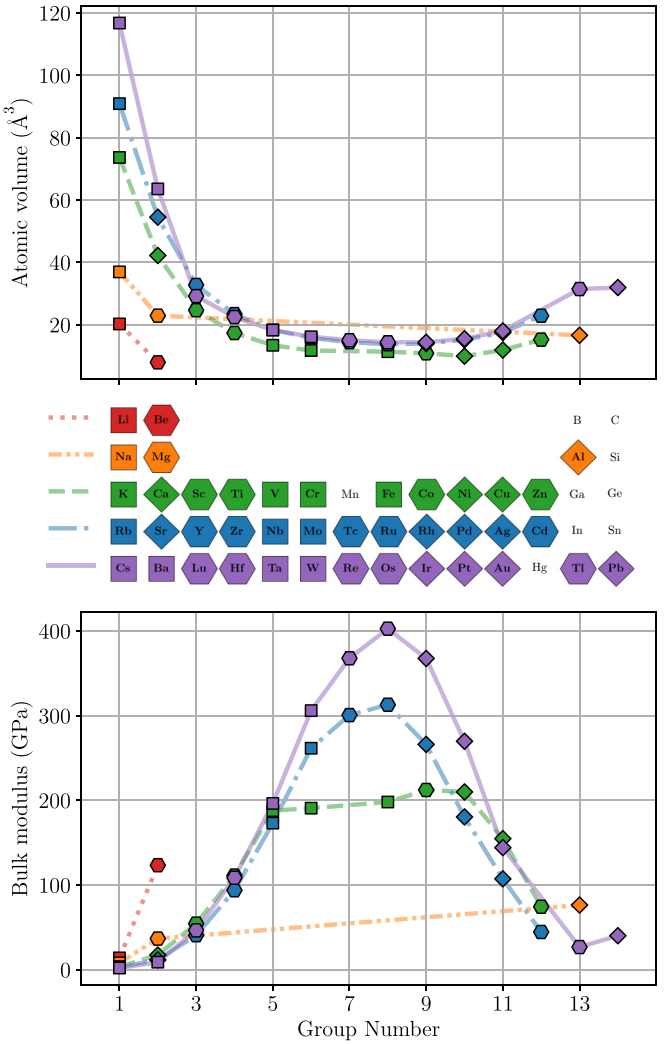


FIG. 16. Variation of atomic volume (top) and bulk modulus (bottom) as a function of group number in the Periodic Table for all the bcc [2], fcc [3], and hcp (this work) elements. Data for fcc Th have been excluded and hcp Lu was treated as a group III element. Lines connect elements of the same period, as shown to the left of the Periodic Table at the center of the figure.

number. On average, vacancy and self-interstitial atom defect relaxation volumes in pure elements fluctuate around ~ -0.35 and ~ 1.46 atomic volumes, respectively, as indicated by Eq. (19). For comparison, in the limit where defects form clusters, for example, voids or dislocation loops, the relaxation volume *per defect* asymptotically approaches -1 atomic volume for vacancy dislocation loops, $+1$ atomic volume for interstitial dislocation loops, and zero for voids [85].

Variation of relaxation volumes of point defects across a given period is similar to other periods. Oscillatory behavior is observed for vacancies with distinct peaks and troughs in groups II, V, and VIII with the exception of bcc vanadium. Self-interstitial atom defects also show a similar variation across periods, although the oscillation period is larger, with a distinct peak and trough at groups VIII and III, respectively. The finer details of these plots may require consideration of high-order moments of the density of states (DOS). The

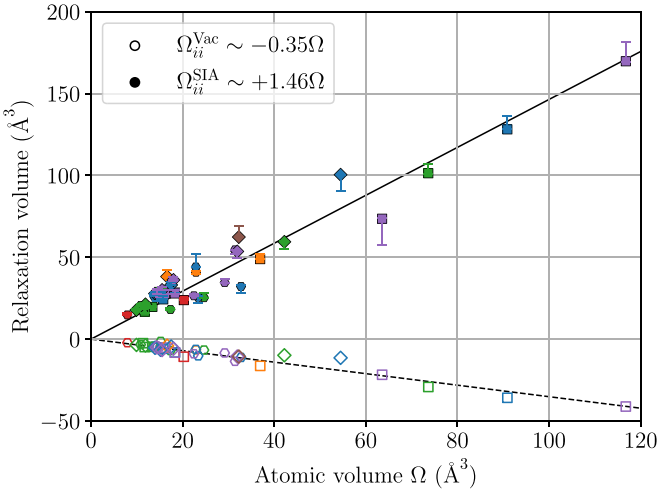


FIG. 17. Traces of SIA and vacancy relaxation volume tensors Ω_{ii} for hcp (this work), bcc [2], and fcc [3] metals plotted against the atomic volume for the respective element. Data points show Ω_{ii} for the lowest-energy SIA configurations, and the error bars indicate the range of variation of defect volumes across all the SIA configurations for that element.

difference in hcp, bcc, and fcc structures requires accounting for high-order moments of the DOS that reveals similar oscillatory behavior with similar periods [86].

No notable trends were identified for the anisotropic parts of the dipole and relaxation volume tensors with respect to electron configuration. This suggests that the anisotropic properties of point defects in metals is most strongly affected by the symmetry of the crystal structure. For example, bcc and fcc vacancies contain no deviatoric components in either their dipole or relaxation volume tensors [2,3]. However, in

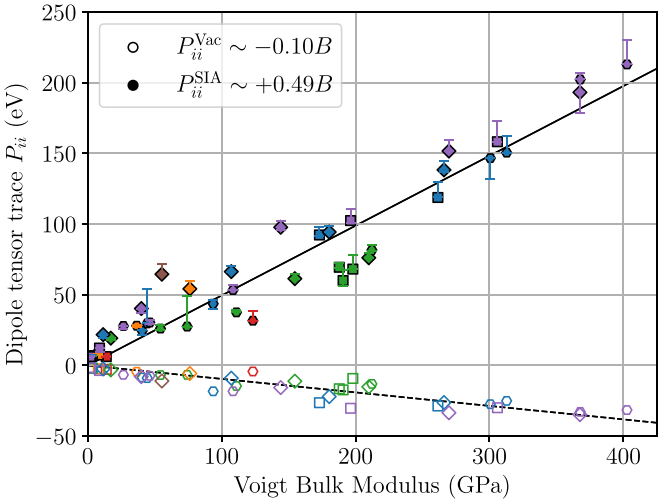


FIG. 18. Traces of SIA and vacancy elastic dipole tensors P_{ii} for hcp (this work), bcc [2], and fcc [3] metals plotted against the Voigt averaged bulk modulus for the respective element. The unit of the correlation coefficient is eV/GPa. Data points show P_{ii}^{SIA} for the lowest-energy SIA configurations, and the error bars indicate the range of variation of defect dipole tensors across all the SIA configurations for that element.

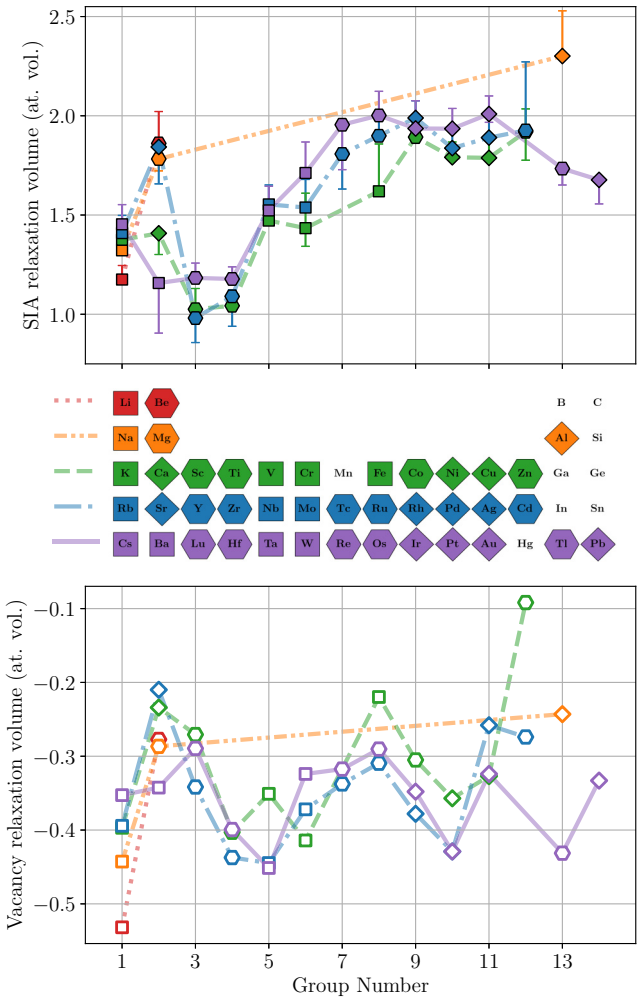


FIG. 19. Lowest energy SIA (top) and vacancy (bottom) relaxation volumes as a function of group number in the Periodic Table for all the bcc [2], fcc [3], and hcp (this work) elements. Error bars indicate the largest and smallest SIA relaxation volume for all the simulated configurations. Data for fcc Th have been excluded and hcp Lu was treated as a group III element. Lines connect elements of the same period, as shown to the left of the Periodic Table at the center of the figure.

hcp metals the deviatoric part can be substantial, as discussed in Sec. III A above.

V. CONCLUSIONS

In this study, we computed elastic dipole and relaxation volume tensors of intrinsic point defects across all the hcp metals in the Periodic Table. This completes the *ab initio* database of point defect properties of hcp, bcc, and fcc metals [2,3] across the entire Periodic Table, except for the lanthanides and actinides. SIA defects show little variation in their relaxation volumes for the configurations considered; it remains to be seen whether lower-symmetry configurations break this trend. For both interstitials and vacancies, we have found a strong correlation between the traces of relaxation volume tensors and dipole tensors with atomic volume and bulk modulus of respective elements. The data reviewed in this study can now be used for predicting radiation-induced deformation [87] of metals currently in service in nuclear power plants, or even full reactor structures [88] operating in extreme radiation environments.

ACKNOWLEDGMENTS

The authors gratefully acknowledge stimulating discussions with M. Boleininger and D. R. Mason. This work has been carried out within the framework of the EUROfusion Consortium, funded by the European Union via the Euratom Research and Training Programme (Grant Agreement No. 101052200–EUROfusion), and was partially supported by the Broader Approach Phase II agreement under the PA of IFERC2-T2PA02. This work was also funded by the UK Fusion Futures Programme and the UK EPSRC Energy Programme (Grant No. EP/W006839/1). To obtain further information on the data and models underlying the paper please contact PublicationsManager@ukaea.uk. Views and opinions expressed are, however, those of the authors only and do not necessarily reflect those of the European Union or the European Commission. Neither the European Union nor the European Commission can be held responsible for them. Numerical calculations were performed using resources provided by the Cambridge Service for Data Driven Discovery (CSD3) operated by the University of Cambridge Research Computing Service and ARCHER 2, the UK National Supercomputing Service.

DATA AVAILABILITY

The data supporting this study's findings are available within the article.

[1] G. Leibfried and N. Breuer, *Point Defects in Metals I*, Springer Tracts in Modern Physics Vol. 81 (Springer-Verlag, Berlin, 1978).

[2] P.-W. Ma and S. L. Dudarev, Universality of point defect structure in body-centered cubic metals, Phys. Rev. Mater. **3**, 013605 (2019).

[3] P.-W. Ma and S. L. Dudarev, Nonuniversal structure of point defects in face-centered cubic metals, Phys. Rev. Mater. **5**, 013601 (2021).

[4] A. P. Sutton, *Physics of Elasticity and Crystal Defects* (Oxford University Press, Oxford, 2020).

[5] D. Nguyen-Manh, A. P. Horsfield, and S. L. Dudarev, Self-interstitial atom defects in bcc transition metals: Group-specific trends, Phys. Rev. B **73**, 020101(R) (2006).

[6] P. Olsson, *Ab initio* study of interstitial migration in Fe–Cr alloys, J. Nucl. Mater. **386-388**, 86 (2009).

[7] P.-W. Ma and S. L. Dudarev, Symmetry-broken self-interstitial defects in chromium, molybdenum, and tungsten, Phys. Rev. Mater. **3**, 043606 (2019).

[8] S. V. S. Prasad, S. B. Prasad, K. Verma, R. K. Mishra, V. Kumar, and S. Singh, The role and significance of magnesium in modern day research—a review, J. Magn. Alloys **10**, 1 (2022).

[9] J. C. Williams and R. R. Boyer, Opportunities and issues in the application of titanium alloys for aerospace components, Metals **10**, 705 (2020).

[10] R. B. Adamson, C. E. Coleman, and M. Griffiths, Irradiation creep and growth of zirconium alloys: A critical review, J. Nucl. Mater. **521**, 167 (2019).

[11] T. Wang, P. Liu, S. Wang, S. Wang, X. Yi, W. Han, Q. Zhan, and F. Wan, A review on irradiated beryllium and beryllium alloy for fusion reactor application: Microstructure evolution, properties changes, and fabrication, Fusion Eng. Des. **211**, 114780 (2025).

[12] R. C. Pasianot, Self-interstitials structure in the hcp metals: A further perspective from first-principles calculations, J. Nucl. Mater. **481**, 147 (2016).

[13] G. Vérité, C. Domain, C.-C. Fu, P. Gasca, A. Legris, and F. Willaime, Self-interstitial defects in hexagonal close packed metals revisited: Evidence for low-symmetry configurations in Ti, Zr, and Hf, Phys. Rev. B **87**, 134108 (2013).

[14] D. J. Oh and R. A. Johnson, Relationship between *c/a* ratio and point defect properties in HCP metals, J. Nucl. Mater. **169**, 5 (1989).

[15] A. M. Monti, Dipole tensors and volume changes of point defects in H.C.P. lattices, phys. status solidi b **168**, 49 (1991).

[16] W. Hu, H. Deng, X. Yuan, and M. Fukumoto, Point-defect properties in HCP rare earth metals with analytic modified embedded atom potentials, Eur. Phys. J. B **34**, 429 (2003).

[17] T. Angsten, T. Mayeshiba, H. Wu, and D. Morgan, Elemental vacancy diffusion database from high-throughput first-principles calculations for fcc and hcp structures, New J. Phys. **16**, 015018 (2014).

[18] S.-L. Shang, B.-C. Zhou, W. Y. Wang, A. J. Ross, X. L. Liu, Y.-J. Hu, H.-Z. Fang, Y. Wang, and Z.-K. Liu, A comprehensive first-principles study of pure elements: Vacancy formation and migration energies and self-diffusion coefficients, Acta Mater. **109**, 128 (2016).

[19] M. S. Nitol, D. E. Dickel, and C. D. Barrett, Artificial neural network potential for pure zinc, Comput. Mater. Sci. **188**, 110207 (2021).

[20] M. Ganchenkova, P. Vladimirov, and V. Borodin, Vacancies, interstitials and gas atoms in beryllium, J. Nucl. Mater. **386-388**, 79 (2009).

[21] L. Ferry, F. Virot, Y. Ferro, D. Matveev, C. Linsmeier, and M. Barrachin, Diffusivity of hydrogen and properties of point defects in beryllium investigated by DFT, J. Nucl. Mater. **524**, 323 (2019).

[22] V. A. Borodin and P. V. Vladimirov, Vacancies and interstitials in yttrium, J. Phys.: Condens. Matter **31**, 185401 (2019).

[23] S. J. Wooding, D. J. Bacon, and W. J. Phythian, A computer simulation study of displacement cascades in α-titanium, Philos. Mag. A **72**, 1261 (1995).

[24] M. Wen, C. H. Woo, and H. Huang, Atomistic studies of stress effects on self-interstitial diffusion in α-titanium, J. Comput.-Aided Mater. Des. **7**, 97 (2000).

[25] A. Tunde Raji, S. Scandolo, R. Mazzarello, S. Nsengiyumva, M. Härting, and D. T. Britton, *Ab initio* pseudopotential study of vacancies and self-interstitials in hcp titanium, Philos. Mag. **89**, 1629 (2009).

[26] S. K. Nayak, C. J. Hung, V. Sharma, S. P. Alpay, A. M. Dongare, W. J. Brindley, and R. J. Hebert, Insight into point defects and impurities in titanium from first principles, npj Comput. Mater. **4**, 11 (2018).

[27] C. K. Ong, Vacancies in α-Zirconium, phys. status solidi b **112**, 312 (1982).

[28] N. de Diego, Y. N. Osetsky, and D. J. Bacon, Mobility of interstitial clusters in alpha-zirconium, Metall. Mater. Trans. A **33**, 783 (2002).

[29] C. Domain and A. Legris, *Ab initio* atomic-scale determination of point-defect structure in hcp zirconium, Philos. Mag. **85**, 569 (2005).

[30] N. de Diego, Y. Osetsky, and D. Bacon, Structure and properties of vacancy and interstitial clusters in α-zirconium, J. Nucl. Mater. **374**, 87 (2008).

[31] N. de Diego, A. Serra, D. J. Bacon, and Y. N. Osetsky, On the structure and mobility of point defect clusters in alpha-zirconium: A comparison for two interatomic potential models, Modell. Simul. Mater. Sci. Eng. **19**, 035003 (2011).

[32] G. Samolyuk, S. Golubov, Y. Osetsky, and R. Stoller, Self-interstitial configurations in hcp Zr: A first principles analysis, Philos. Mag. Lett. **93**, 93 (2013).

[33] Q. Peng, W. Ji, H. Huang, and S. De, Stability of self-interstitial atoms in hcp-Zr, J. Nucl. Mater. **429**, 233 (2012).

[34] Q. Peng, W. Ji, H. Huang, and S. De, Axial ratio dependence of the stability of self-interstitials in HCP structures, J. Nucl. Mater. **437**, 293 (2013).

[35] M. Christensen, W. Wolf, C. Freeman, E. Wimmer, R. Adamson, L. Hallstadius, P. Cantonwine, and E. Mader, Diffusion of point defects, nucleation of dislocation loops, and effect of hydrogen in hcp-Zr: *Ab initio* and classical simulations, J. Nucl. Mater. **460**, 82 (2015).

[36] G. Samolyuk, A. Barashev, S. Golubov, Y. Osetsky, and R. Stoller, Analysis of the anisotropy of point defect diffusion in hcp Zr, Acta Mater. **78**, 173 (2014).

[37] Q. Peng, W. Ji, J. Lian, X.-J. Chen, H. Huang, F. Gao, and S. De, Pressure effect on stabilities of self-Interstitials in HCP-Zirconium, Sci. Rep. **4**, 5735 (2015).

[38] C. Varvenne and E. Clouet, Elastic dipoles of point defects from atomistic simulations, Phys. Rev. B **96**, 224103 (2017).

[39] X. Li, Y. Qin, J. Fu, and J. Zhao, A Gupta potential for magnesium in hcp phase, Comput. Mater. Sci. **98**, 328 (2015).

[40] K. Fan, J. Tang, Q. Sun, S. Wu, and X. Wang, First-principles study on the properties of point defects in Hcp-Dy, in *Proceedings of the International Conference on Advances in Energy, Environment and Chemical Engineering* (Atlantis Press, Paris, France, 2015).

[41] K. Fan, L. Yang, S. M. Peng, X. G. Long, Z. Wu, and X. T. Zu, Analytical Interatomic Potential for HCP-Scandium, Mater. Sci. Forum **689**, 39 (2011).

[42] D. J. Bacon, Point defects and clusters in the hcp metals: their role in the dose transition, J. Nucl. Mater. **206**, 249 (1993).

[43] D. J. Bacon, R. Bullough, and J. R. Willis, The anisotropic elastic energy of a rhombus-shaped dislocation loop, Philos. Mag. **22**, 31 (1970).

[44] J. F. Nye, *Physical Properties of Crystals: Their Representation by Tensors and Matrices* (Oxford University Press, Oxford, 1985).

[45] W. Cai and W. D. Nix, *Imperfections in Crystalline Solids* (Cambridge University Press, Cambridge, 2016).

[46] S. L. Dudarev, D. R. Mason, E. Tarleton, P.-W. Ma, and A. E. Sand, A multi-scale model for stresses, strains and swelling of reactor components under irradiation, Nucl. Fusion **58**, 126002 (2018).

[47] A. M. Kossevich, *The Crystal Lattice* (Wiley-VCH, Weinheim, 2005).

[48] C. Varvenne, F. Bruneval, M.-C. Marinica, and E. Clouet, Point defect modeling in materials: Coupling *ab initio* and elasticity approaches, Phys. Rev. B **88**, 134102 (2013).

[49] S. Han, L. A. Zepeda-Ruiz, G. J. Ackland, R. Car, and D. J. Srolovitz, Self-interstitials in V and Mo, Phys. Rev. B **66**, 220101(R) (2002).

[50] J. W. Arblaster, *Selected Values of the Crystallographic Properties of the Elements* (ASM International, New York, 2018).

[51] G. Kresse and J. Hafner, *Ab initio* molecular dynamics for liquid metals, Phys. Rev. B **47**, 558 (1993).

[52] G. Kresse and J. Hafner, *Ab initio* molecular-dynamics simulation of the liquid-metal–amorphous-semiconductor transition in germanium, Phys. Rev. B **49**, 14251 (1994).

[53] G. Kresse and J. Furthmüller, Efficiency of *ab initio* total energy calculations for metals and semiconductors using a plane-wave basis set, Comput. Mater. Sci. **6**, 15 (1996).

[54] G. Kresse and J. Furthmüller, Efficient iterative schemes for *ab initio* total-energy calculations using a plane-wave basis set, Phys. Rev. B **54**, 11169 (1996).

[55] G. Kresse and J. Hafner, Norm-conserving and ultrasoft pseudopotentials for first-row and transition elements, J. Phys.: Condens. Matter **6**, 8245 (1994).

[56] G. Kresse and D. Joubert, From ultrasoft pseudopotentials to the projector augmented-wave method, Phys. Rev. B **59**, 1758 (1999).

[57] See Supplemental Material at http://link.aps.org/supplemental/10.1103/qmfp-j51l for plane wave energy cut-off and *k*-point mesh convergence test data and the variation of point defect elastic dipole tensors with the number atoms in a supercell for the hexagonal close packed metals considered in this work.

[58] J. P. Perdew, K. Burke, and M. Ernzerhof, Generalized gradient approximation made simple, Phys. Rev. Lett. **77**, 3865 (1996).

[59] J. P. Perdew, A. Ruzsinszky, G. I. Csonka, O. A. Vydrov, G. E. Scuseria, L. A. Constantin, X. Zhou, and K. Burke, Restoring the density-gradient expansion for exchange in solids and surfaces, Phys. Rev. Lett. **100**, 136406 (2008).

[60] G. Simmons and H. Wang, *Single Crystal Elastic Constants and Calculated Aggregate Properties*, 2nd ed. (The MIT Press, Cambridge, MA, 1971).

[61] J. J. Tonnies, K. A. Gschneidner, Jr., and F. H. Spedding, Elastic moduli and thermal expansion of lutetium single crystals from 4.2 to 300 °K, J. Appl. Phys. **42**, 3275 (1971).

[62] C. Pantea, I. Stroe, H. Ledbetter, J. B. Betts, Y. Zhao, L. L. Daemen, H. Cynn, and A. Migliori, Elastic constants of osmium between 5 and 300 K, Phys. Rev. B **80**, 024112 (2009).

[63] R. G. Leisure, R. B. Schwarz, A. Migliori, and M. Lei, Room-temperature elastic constants of Sc and $ScD_{0.18}$, Phys. Rev. B **48**, 1276 (1993).

[64] A. F. Guillermet and G. Grimvall, Thermodynamic properties of technetium, J. Less-Common Met. **147**, 195 (1989).

[65] Y. Le Page and P. Saxe, Symmetry-general least-squares extraction of elastic data for strained materials from *ab initio* calculations of stress, Phys. Rev. B **65**, 104104 (2002).

[66] X. Wu, D. Vanderbilt, and D. R. Hamann, Systematic treatment of displacements, strains, and electric fields in density-functional perturbation theory, Phys. Rev. B **72**, 035105 (2005).

[67] H. P. Myers and W. Sucksmith, The spontaneous magnetization of cobalt, Proc. R. Soc. London A **207**, 427 (1997).

[68] S. L. Dudarev and P.-W. Ma, Elastic fields, dipole tensors, and interaction between self-interstitial atom defects in bcc transition metals, Phys. Rev. Mater. **2**, 033602 (2018).

[69] P.-W. Ma and S. L. Dudarev, CALANIE: Anisotropic elastic correction to the total energy, to mitigate the effect of periodic boundary conditions, Comput. Phys. Commun. **252**, 107130 (2020).

[70] *International Tables for Crystallography: Space-Group Symmetry*, 2nd ed., edited by M. I. Aroyo (International Union of Crystallography, Chester, UK, 2016), Vol. A.

[71] E. Clouet, S. Garruchet, H. Nguyen, M. Perez, and C. S. Becquart, Dislocation interaction with C in α-Fe: A comparison between atomic simulations and elasticity theory, Acta Mater. **56**, 3450 (2008).

[72] D. G. Pettifor, *Bonding and Structure of Molecules and Solids* (Clarendon Press, Oxford, 1995).

[73] N. Gaston, D. Andrae, B. Paulus, U. Wedig, and M. Jansen, Understanding the hcp anisotropy in Cd and Zn: The role of electron correlation in determining the potential energy surface, Phys. Chem. Chem. Phys. **12**, 681 (2010).

[74] S. L. Dudarev, Density functional theory models for radiation damage, Annu. Rev. Mater. Res. **43**, 35 (2013).

[75] *Atomic Defects in Metals*, Landolt-Börnstein-Group III Condensed Matter, edited by H. Ullmaier (Springer-Verlag, Berlin, 1991), Vol. 25.

[76] A. Seeger, Vacancies and self-interstitials in zinc and cadmium, Philos. Mag. A **64**, 735 (1991).

[77] P. Ehrhart and B. Schönfeld, Investigation of electron-irradiated zinc by diffuse X-ray scattering. I. Self-interstitials in zinc, Phys. Rev. B **19**, 3896 (1979).

[78] P.-W. Ma and S. L. Dudarev, Effect of stress on vacancy formation and migration in body-centered-cubic metals, Phys. Rev. Mater. **3**, 063601 (2019).

[79] Y. Kraftmakher, Equilibrium vacancies and thermophysical properties of metals, Phys. Rep. **299**, 79 (1998).

[80] *CRC Handbook of Chemistry and Physics*, 92nd ed., edited by W. M. Haynes (CRC Press, Boca Raton, FL, 2011).

[81] C. Lapointe, T. D. Swinburne, L. Thiry, S. Mallat, L. Proville, C. S. Becquart, and M.-C. Marinica, Machine learning surrogate models for prediction of point defect vibrational entropy, Phys. Rev. Mater. **4**, 063802 (2020).

[82] G. Lucas and R. Schäublin, Vibrational contributions to the stability of point defects in bcc iron: A first-principles study, Nucl. Instrum. Methods Phys. Res. Sect. B **267**, 3009 (2009).

[83] C. Freysoldt, B. Grabowski, T. Hickel, J. Neugebauer, G. Kresse, A. Janotti, and C. G. Van de Walle, First-principles calculations for point defects in solids, Rev. Mod. Phys. **86**, 253 (2014).

[84] J. Kübler, *Theory of Itinerant Electron Magnetism* (Clarendon Press, Oxford, UK, 2000).

[85] D. R. Mason, D. Nguyen-Manh, M.-C. Marinica, R. Alexander, A. E. Sand, and S. L. Dudarev, Relaxation volumes of microscopic and mesoscopic irradiation-induced defects in tungsten, J. Appl. Phys. **126**, 075112 (2019).

[86] M. Aoki and D. G. Pettifor, Directional bonding in atomistic simulations, Mater. Sci. Eng.: A **176**, 19 (1994).

[87] L. Reali, M. Boleininger, M. R. Gilbert, and S. L. Dudarev, Macroscopic elastic stress and strain produced by irradiation, Nucl. Fusion **62**, 016002 (2022).

[88] W. M. E. Ellis, L. Reali, A. Davis, H. M. Brooks, I. Katramados, A. J. Thornton, R. J. Akers, and S. L. Dudarev, Mechanical model for a full fusion tokamak enabled by supercomputing, Nucl. Fusion **65**, 036033 (2025).